Subcooled forced convection boiling flow measured using high-resolution techniques at the COSMOS-L facility and accompanying CFD simulation employing an interface-tracking scheme

Florian Kaiser [a], Yohei Sato [b], Stephan Gabriel [a,*]

[a] *Karlsruhe Institute of Technology, Germany*
[b] *Paul Scherrer Institute, Switzerland*

Keywords:
Subcooled boiling
Critical heat flux
Boiling crisis
Two phase flow
Interface tracking

A B S T R A C T

This paper describes state-of-the-art experimental measurement techniques and computational fluid dynamics methods applied to subcooled forced convection boiling flow at 2-3 *bar*, both featuring high spatial- and time-resolution measurements. The objectives are: (i) to provide the measured boiling flow data, e.g. average and RMS profiles of axial and radial velocities and bubble size distributions, and (ii) to evaluate the capabilities of state-of-the-art numerical simulation techniques to model the observed phenomena, by comparison between measured data and numerical prediction. In the experiment, the bubble velocities in the axial and radial directions were measured using laser Doppler anemometry, and the bubble size was estimated by a shadowgraphy method. The simulation results, incorporating an interface capturing technique, showed good agreement with measurement in terms of the wall temperature and axial velocity, but underestimation of the radial velocity, and overestimation of bubble sizes. The paper shows that the discrepancies between measurement and simulation may be traced to: (i) the uncertainties in the nucleation site density model; (ii) too coarse a grid being adopted, which is not able to resolve the thermal boundary layer around the bubbles; and (iii) spurious numerical bubble coalescence, a feature not seen in the experiment. The mechanism of bubble lift-off from the hot surface, without any sliding motion, as observed in the experiment, is discussed in detail, based on the simulation results, and the condensation on the bubble cap as the bubble is 'sucked' into the bulk flow is also examined.

1. Introduction

Boiling heat transfer is used in a variety of engineering applications: e.g. nuclear power plants, refrigerators, heat pipes and chemical processing devices. Important parameters are the overall heat transfer coefficient and the maximum heat flux the so-called Critical Heat Flux, CHF and have been intensively studied in this field, for the purpose of effective, efficient and safe operation of the different systems. Boiling heat transfer and CHF have been measured mainly using thermocouples, and associated empirical correlations and look-up tables have been assembled for the purpose of design and operation of the various applications: e.g. Levy (1959) and Rohsenow (1971). In addition, to better understand the mechanisms of boiling flow and boiling heat transfer, measurement techniques have been developed which can resolve local temperatures, velocities and void-fractions (Dhir, 1998). In parallel to the measurements being carried out, Computational Fluid Dynamics, CFD, simulations have been specifically developed to model boiling flows, in order to understand the phenomena taking place, and to simulate boiling heat transfer under various imposed conditions. As a consequence of these techniques, with high resolution, local phenomena relating to boiling flow and boiling heat transfer have been measured, and simulated, in order to gain insights into the physics controlling CHF. In this paper, we present state-of-the-art measurements, and associated CFD simulations, for subcooled, forced-convection boiling flow, and discuss the capabilities and the limitations of the numerical modelling potential.

1.1. Measurements of boiling flow

Numerous measurement methods and instruments have been developed to quantify boiling flows. To produce CFD-grade validation data, accurate measurements are required for the dispersed gas phase

* Corresponding author.
E-mail address: stephan.gabriel@kit.edu (S. Gabriel).

and the continuous liquid phase. In the case of the gaseous phase, the focus is principally on the bubble size and number density, as well as on their trajectories and velocities. The continuous liquid phase is characterized by its velocity and temperature distributions, and on its turbulent properties. The choice of measurement technique, though as always based on the concept of the ideal, is limited by numerous technical and physical restrictions. In general, non-intrusive measurement techniques are to be preferred, to avoid disturbing the morphology of the flow, and optical accessibility of the flows under investigation is limited, especially at high vapor fractions, where refraction and diffraction significantly reduce accessibility in the visible light range. Methods such as high-speed videometry should also be mentioned here, where, for example, images can be generated using the shadow method (Gabriel et al., 2018), which can be processed into discrete measured values using the methods of digital image processing. For a system with multiple cameras, this offers good access to the flow even at high bubble densities (Büttner et al., 2018).

In particular, laser-based methods, such as Laser Doppler Anemometry, LDA, and Particle Image Velocimetry, PIV, e.g. Gabriel (2014), can be used to obtain velocity data and information on the turbulence characteristics of continuous flow situations. Both methods face challenges in the investigation of boiling flows, however, since in the conventional set-up they require the presence of tracer particles in the flow to mark the fluid motion. In addition to the question of whether these particles also act as heterogeneous boiling nuclei in a boiling flow situation, the question also arises of whether a tracer can be found that represents the flow well enough in terms of its density and tracing ability without physically interfering with it. Due to temperature gradients in the flow, as well as the phenomena of evaporation and condensation, this idealization can probably only be achieved in an approximate way.

With respect to the measurement of the phase distribution, other non-intrusive possibilities exist, such as ultrafast X-ray tomography (Fischer and Hampel, 2010). Use of this measurement technique allows a temporally and spatially high-resolution view into the depth of the flow to be obtained. In the field of intrusive measurement, different techniques have been proposed in the context of the quantification of dispersive/boiling flows. The sensors or probes commonly adopted mostly utilize optical or electrical/capacitive methods to detect bubbles and their properties, such as bubble size and velocity. Examples are fiber optic probes that reflect an injected laser beam, based on the different refractive indices of the vapor and liquid phases, and direct it to a photodiode, or not, depending on the fluid present (Bruder et al., 2019). The phase fraction at the discrete location of the probe tip can then be determined by evaluating the time curve of the luminosity signal received by the photo diode.

Apart from the optical sensors, there are further possible measuring techniques, of which at least the two electrical ones should be mentioned. Two electrodes are placed in the flow at a small distance apart; the actual arrangement can vary depending on the experimental set-up. If the liquid phase is electrically conductive and the gas phase is not, the electrical resistance between the two electrodes can be measured continuously. Also, in this case, the phase distribution can be calculated from temporal analysis of the measurement signal. For a non-conductive fluid, it is also possible to use its electrical capacity for measurement. A probe of this type, with a single measuring site, has already been used by Stäbler (2007). The significantly more complex wire mesh sensors (Prasser, 1999) have a much higher number of measuring points, and can record the phase distribution in an entire flow channel. For these sensors, wires are stretched in two planes orthogonal to each other. The measuring sites are located at the intersection points of two cross-wires, and are scanned by the measuring electronics in sequence. A disadvantage of the method is that the probe body itself interacts with the flow, and small bubbles cannot always be detected in some cases (Tompkins et al., 2018).

1.2. Numerical simulation methods for boiling

In boiling flow simulations, it is essential to resolve liquid-vapor interface morphology and area, because vaporization and condensation rates are strongly influenced by the heat flux at the liquid/vapor interface (Sato et al., 2018). Thus, an interface tracking approach, which is able to resolve the liquid-vapor interface, is considered to be the most appropriate for simulations with phase-change phenomena (Yadigaroglu, 2005), although fine computational meshes are required to specifically resolve the interface itself. There are several types of interface tracking approaches: e.g. the Arbitrary Lagrangian-Eulerian, ALE, approach (Fuchs et al., 2006; Lee and Nydahl, 1989; Welch, 1998), the Level Set, LS, method (Huber et al., 2017; Son et al., 1999), the Volume Of Fluid, VOF, method (Kunkelmann and Stephan, 2009; Welch and Wilson, 2000), the Color Function Method, CFM, (Giustini et al., 2017; Murallidharan et al., 2016; Sato and Niceno, 2013), the Front Tracking Method, FTM, (Esmaeeli and Tryggvason, 2004), and the Phase Field Method, PFM, (Badillo, 2012; Jamet et al., 2001; Takada and Tomiyama, 2007). The differences between these approaches stem from the procedure adopted to represent the gas-liquid interface, though all have been used successfully to simulate nucleate boiling and film boiling, as reviewed for example by Kharangate and Mudawar (2017). However, boiling simulations at high heat flux, i.e. near CHF, are rare, because (i) the flow field becomes violent, due to the high mass-transfer rate, which introduces numerical instability, and (ii) an appropriate nucleation site model at high heat flux is required (Sato and Niceno, 2018), a situation that requires further study.

A nucleate pool boiling simulation near CHF has been performed by Son and Dhir (2008), in which multiple nucleation sites were incorporated, with the liquid-vapor interface captured using the LS method. Due to the restriction imposed by the authors of constant temperature over the heat-transfer surface, the bubble waiting time, i.e. the time interval between bubble departure and subsequent bubble nucleation, could not be directly computed, and had to be prescribed *a priori*. Nonetheless, the authors were able to obtain acceptable results for nucleate pool boiling of water for applied heat fluxes up to 800 kW/m^2 at atmospheric pressure. Li et al. (2015) and (Gong and Cheng, 2015), (Gong and Cheng, 2016) have simulated the transition from nucleate boiling to film boiling regimes through CHF using a Lattice-Boltzmann approach. In these works, the influence of the wettability of the heat-transfer surface on the heat transfer coefficient was specifically taken into account. However, the computations are limited to two dimensions, and no validation experiment has been reported. Utilizing the sharp-interface, phase-change model of Sato and Niceno (2013), and its associated depletable micro-layer model (Sato and Niceno, 2015), the authors of these works were able to simulate the pool boiling experiment of Gaertner (1965) from the discrete-bubble regime to the film-boiling regime through to Departure from Nucleate Boiling, DNB; Sato and Niceno (2017), (2018). Unlike the simulation undertaken by Son and Dhir (2008), in these studies, the wall temperature was not prescribed *a priori*, and the computed heat transfer coefficient was in good agreement with experimental data. In the present paper, we apply the same simulation method originally developed for pool boiling flows by Sato and Niceno (2018) to a subcooled, forced-convection boiling flow, and present comparisons with the experimental measurements taken at the COSMOS-L facility.

1.3. Objectives of the current study

In this paper, we present state-of-the-art measurement and simulation results for subcooled, forced-convection boiling flow, to demonstrate recent progress in this field. The measurements were performed at the COSMOS-L loop at the Karlsruhe Institute of Technology, KIT; Haas (2012), Haas et al. (2018). Bubble shapes/motions were measured using high-speed video cameras, and local velocities by Laser Doppler Anemometry, LDA. The measurement of local quantities with high

temporal and spatial resolution enables us to directly compare with numerical simulations. The CFD calculations were performed at the Paul Scherer Institute, PSI, using the in-house, open-source CFD code PSI--BOIL[1], which employs an interface tracking technique. The supercomputer at the Swiss National Supercomputing Centre, CSCS, was employed for the computations. The measured and computed results, e. g. profiles of void fraction, velocity and bubble size distribution, are compared, in order to clarify any limitations and open issues in the both the experimental data and simulation results.

The limitation of the current study is different topology of the test section, which is a double tube in the experiment while a rectangular in the CFD simulations. This is due to the restriction of the CFD code, which can only employ an orthogonal Cartesian grid. Although the dimensions of the test section, i.e. the axial length, circumferential/lateral length, and the gap between the heated surface and the wall on the other side, are same between the experiment and CFD, the ratio of the volume of the channel to the area of the heat transfer surface by 30%. In addition, we infer that the velocity profiles in the wall normal direction differ even for single-phase liquid flow, i.e., the peak appears in the center in the rectangular domain, while it is shifted to the outward in the double-tube domain.

The structure of this paper is as follows: the test facility and measurement methods are described in Section 2, and the CFD simulation method is presented in Section 3, which includes a parametric and grid-dependence study. The measurement and simulation results are compared and discussed in Section 4, and overall conclusions presented in Section 5.

2. Test facility and measurement techniques

2.1. Test facility

The experiments were carried out at the COSMOS-L (Critical-heat-flux On Smooth and MOdified Surfaces – Low pressure) test facility located at the Institute of Thermal Energy Technology and Safety, ITES, of KIT. COSMOS-L is a low pressure water loop for thermo-hydraulic experiments of two-phase flow with heat and mass transfer, operating at low pressure, ranging from 1 to 3 *bar*. The loop was designed to measure the flow under DNB-type CHF conditions, the fluid to the test section inlet being liquid subcooled water; the heated section is most probably not long enough for dryout-type CHF. The working fluid in the present case was deionized water. Electrical conductivity and the oxygen content were continuously monitored during the experiments.

The layout of the facility, i.e. the Piping and Instrumentation Diagram (P&ID), is presented in Fig. 1. First traversing a flow meter (F), the water flows through a preheater, where the fluid temperature is adjusted to a defined level before entering the test section. The mass flow at the test section is set by a control valve, situated between the preheater and the test section.

The test section itself consists of inner and outer tubes, the working fluid flowing vertically upwards through the annular gap between them. The inner tube is made of Zircaloy-4, and it is electrically heated. The outer diameter of the inner tube is 9.5 *mm,* and the thickness of the tube itself is 0.57 *mm*. The outer tube is made of glass, for the purposes of optical measurement. The inner diameter of the glass tube is 18.0 *mm*, and the thickness of glass is 2 *mm*. Fig. 2 shows the cross-section of the test section (right) and a photograph of the assembled test section (left). Referring to the bottom of Fig. 2 (left), the water enters the inlet block from four sides, each connected to a high pressure hose, and is then directed upwards into the unheated annular section. The lower copper part of the inner test tube is centered in the inlet block by a ring with four spacers. The ring is made of the thermoplastic material PEEK (Polyether ether ketone), which also insulates against electrical contact between the heated section and the pressure hull. The glass tube is sealed by an O-ring, and centered by the PEEK ring in the inlet block. The heated section begins where the fluid enters the annular channel formed by the central Zircaloy-4 tube and the glass tube surround. The heated inner tube has a length of 326 *mm*. The test section is connected to the outlet block, and the working fluid then flows into a large horizontal channel of diameter 100 *mm*. The vapor and liquid phases separate from each other in the condenser downstream of the outlet block, Fig. 1. The glass tube and the upper copper conductor, are both centered, and sealed, in the outlet section. Outside of the test section, flexible cables for the power supply are connected to the bottom and top ends of the inner tube assembly. The inlet block is fixed and positioned relative to the outlet assembly as a notionally "stiff" structure.

2.2. Measurement apparatus

2.2.1. Thermocouples and pressure sensors

The loop is equipped with several temperature and pressure sensors, as indicated in Fig. 1, the test section itself being equipped with sensors for such measurements. A lance, consisting of twelve thermocouples, is inserted into the zircaloy tube, as shown in Fig. 3. In addition to temperature measurement, an important function of the thermocouples is the detection of CHF, which is explained in section 2.3 below. The thermocouples are of type K, with a diameter of 0.36 *mm*. The pressures at the inlet and outlet block were continuously monitored, the outlet pressure being considered the system pressure.

The positions of the thermocouples are illustrated in Fig. 2 (right). At each height, two thermocouples are placed on opposite sides of the inside of the zircaloy tube. The height distribution has been chosen according to the experience gained from the determination of CHF in earlier experiments. For the chosen test section gap (8.5 mm), CHF was observed mostly at the very top of the test section in the experiments reported here.

2.2.2. High speed video camera

Using video cameras, it is possible to observe the liquid-vapor interface during the test; i.e. bubble growth, bubble motion and vapor agglomerations. A standard action camera with a frame rate of 30 *fps*, and a resolution of 3840 $\times$ 2160 pixels, is used for the overall observation of the test section, in particular continuous observation of the upper part. For the purposes of observing transient phenomena at high resolution, three high-speed video cameras were installed at different axial height positions, as illustrated in Fig. 4. The framerate was 3000 *fps,* with a resolution of 1280 $\times$ 1024 pixels.

2.2.3. LDA for bubble size and bubble velocity measurement

Bubble sizes and bubble velocities are essential for mechanistic model descriptions. The measurement of these parameters allows a direct comparison with the predicted values of the different model theories to be made, and represent important quantities for the validation of such models. In addition, the local vapor content plays a key role in all models, as it hinders the supply of fresh cooling medium to the heated surface, and can thus promote CHF conditions.

The outer glass tube enabled the application of further optical measurement technologies to be utilized. The choice of measurement method needs to be made carefully to avoid the influence of the physical presence of in-situ measurement devices, e.g. probes or wire meshes, on the boiling process. Thus, only non-invasive methods have been used in the tests reported here. The vapor bubble velocities were measured using a LDA system. A Diode-Pumped Solid-State Laser, DPSSL, with the maximum power of 300 *mW* and wavelength of 532 and 561 *nm,* having been was employed. A focal lens of 300 *mm* was used, providing a measuring volume of 0.7 mm^3. In order to avoid disturbance of the flow by the use of tracer particles, only small bubbles ($\sim$100 μm) of steam, or small amounts of non-condensable gases, were used as tracers. The measurement times are defined in such a way as to ensure a sufficient

[1] https://github.com/Niceno/PSI-BOIL.

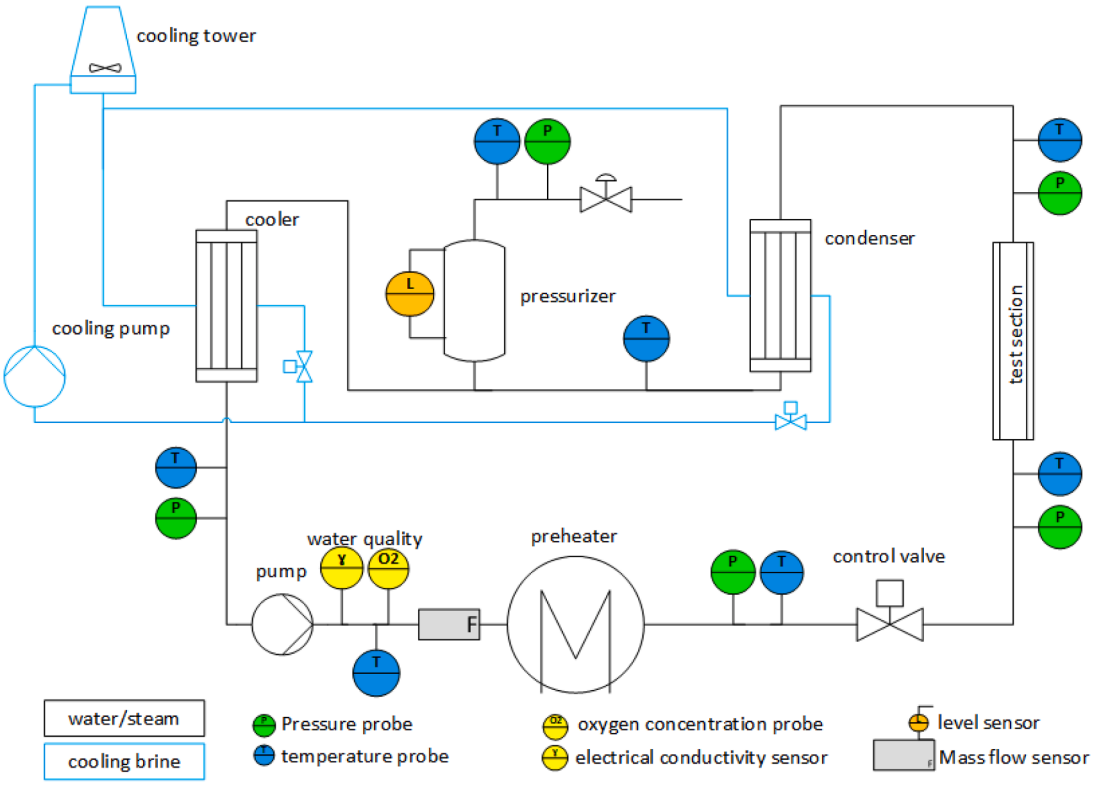

Fig. 1. Piping and instrumentation diagram of the COSMOS-L facility.

number of measured values are recorded at each measurement point, in order to make a reliable estimate of the mean value, and to determine the measurement uncertainty. The optical refraction at the transition between the water and the outer glass tube was taken into account by calibration of the optical system, and a correction function derived from it. Velocity profiles ranging from 0.06 $mm \leq r \leq 4.3$ *mm,* with an interval of 0.07 *mm,* were measured at all three positions: Positions 1, 2 and 3 in Fig. 4. A comparison of the estimated mass flow rate based on LDA, and the superficial velocity measured by the flow meter upstream of the test section, was undertaken continuously during the experiment (Fig. 5).

In addition to the bubble velocities, the bubble size distribution has also been measured in the tests. To this purpose, a shadowgraphy method was employed. However, due to frequent bubble coalescence processes, and the rapid evaporation and condensation of the bubbles, simultaneous detection of the bubble sizes and the velocities proved to be unachievable. It was observed that the bubbles that formed the heated surface deformed so rapidly that an automated assignment of the bubbles on double images was not possible. The time differences between the double images had to be chosen large enough to ensure that the bubbles move by a measurable distance, but the deformation of the bubbles within this period proved to be too large, which prevented the alignment to be achieved. Therefore, the velocity measurements were carried out using LDA instead, focusing on the small bubbles already present in the flow at the designated measurement locations. The set-up of the shadowgraphy measurements is shown in Fig. 6. An Nd:YAG laser provides the illumination required, prepared by a diffusor and several matt screens, resulting in a homogeneous background illumination. On the opposite site of the test section, a Charge-Coupled Device, CCD, camera had been placed, which registers an image of the flow in which bubbles appear darker than the continuous liquid, due to light refractions. Such images were taken at a frequency of 2 *Hz*. For any given bubble distribution, a minimum of 50 images needed to be taken into consideration. The observation time for the images corresponds in total to 250 *s,* within which the images are taken at equidistant time intervals, to avoid over-interpretation of exceptional flow events.

2.3. *Measurement procedure*

First, the CHF condition was determined a priori by performing a series of experiments under different boundary conditions. Knowing the value of the critical heat flux, and the frequency distribution for the critical power from a large number of pre-test experiments, the boiling characteristics of the test section could be estimated at reduced heating power in relation to the critical CHF power. This was achieved using the same boundary conditions (pressure, inlet fluid temperature/subcooling and mass flow rate). A steady-state measurement under CHF conditions is impossible in water, since CHF induces a high temperature increase on the heater surface with a gradient of about 200 K/s. The heater would then be damaged in a short time. The criterion for CHF estimation is based here on the prerequisite that CHF occurs spontaneously at a specific applied power level. In addition to a temperature criterion, a time criterion is defined within which CHF can occur. Each level of heating power was applied for two minutes before the next increment was initiated. Within these two minutes, the thermal-hydraulic parameters had been observed to stabilize to the extent that a quasi-stationary flow situation could be assumed.

When CHF conditions are reached, a rapid shutdown of the heating power must be triggered, in order to protect the test section from damage. However, within the short time span between the heating power increase and the occurrence of CHF, no reproducible measurement of thermal-hydraulic parameters could be realized. Therefore, specifically defined plateaus of the heating power had to be selected, for which a more detailed measurement of the parameters could be carried out. Consequently, a measuring point was selected corresponding to an inlet temperature of $T_{in} = 80°C$, mass flux of $G = 400\ kg/(m^2\ s)$, and a system pressure at the outlet of the test section of 2 *bar*. This is equivalent to a thermal subcooling of 40.2 *K*. CHF for this case was found to be 1.23 MW/m^2. Thermal-hydraulic parameters were adjusted at 50% of this heating power, corresponding to CHF at the top of the test section.

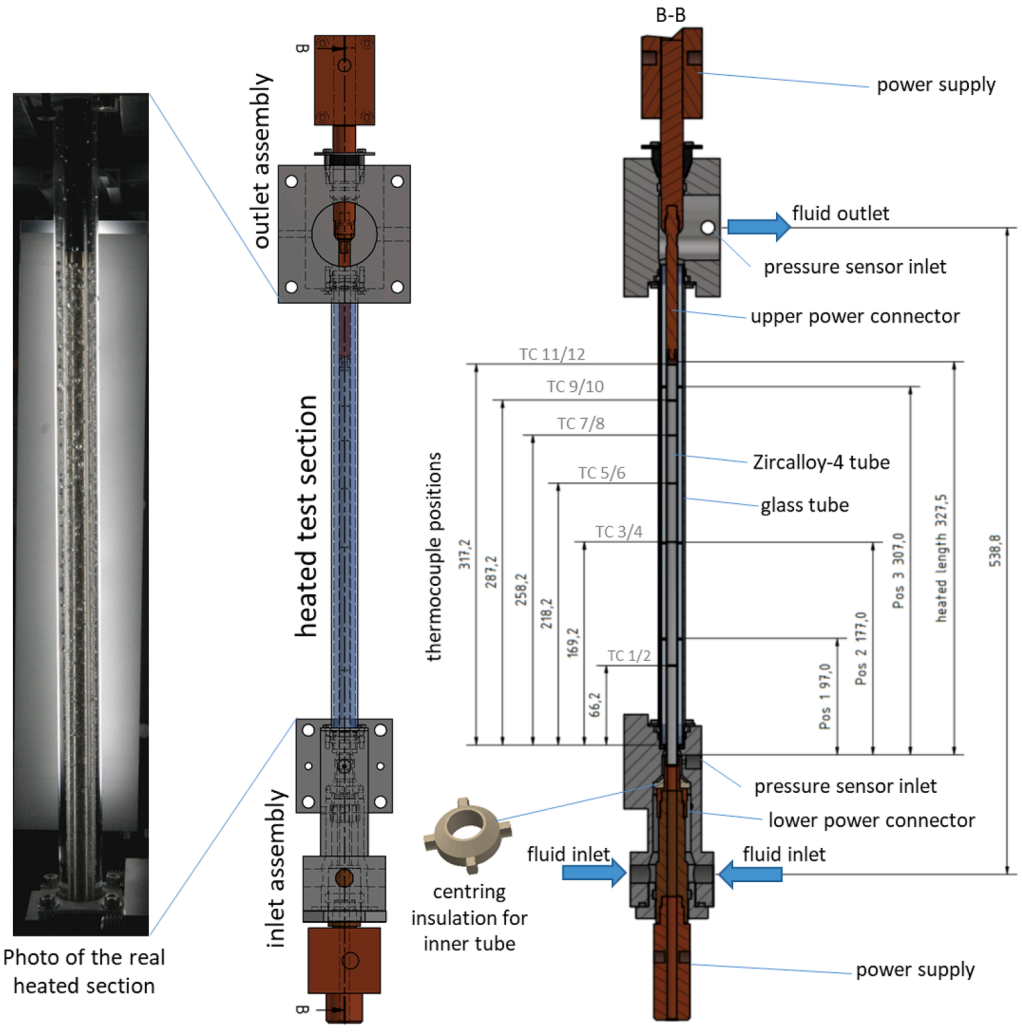

Fig. 2. Photo (left) and schematic (right) of the annular test section of COSMOS-L.

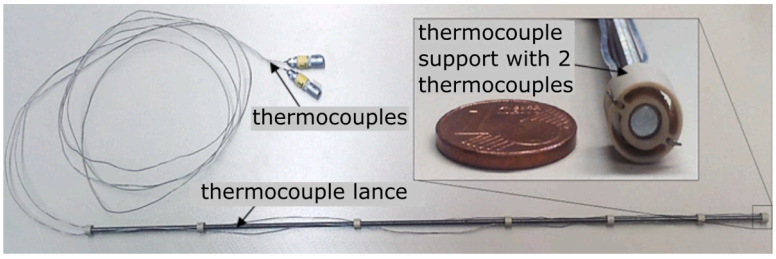

Fig. 3. Lance of thermocouples inserted into the inner tube.

3. CFD simulation method

The numerical method used for the CFD simulations is briefly explained here. The open-source CFD code, PSI-BOIL, is employed for all the simulations. The vapor and liquid phases are assumed to be incompressible fluids, and the solid phase is incorporated according to the immersed boundary method (Mittal and Iaccarino, 2005). The method is essentially the same as that developed for the pool boiling flow simulations of Sato and Niceno (2017, 2018), the difference being that the presence of inlet and outlet boundaries for forced convective flow in the present context. Detailed explanations of the fluid flow equations solver with mass transfer are given in Sato and Niceno (2013), and the modelling for nucleation sites and micro-layer development are explained in Sato and Niceno (2015, 2018). The parametric study conducted for the nucleation site density modelling, and grid dependency study, are presented in this paper, together with the simulation results specifically in the context the COSMOS-L facility.

3.1. Governing equations

The governing equations may be written (Sato and Niceno, 2013):

$$\nabla\cdot\vec{u} = \left(\frac{1}{\rho_v} \quad \frac{1}{\rho_l}\right)\dot{m} \tag{1}$$

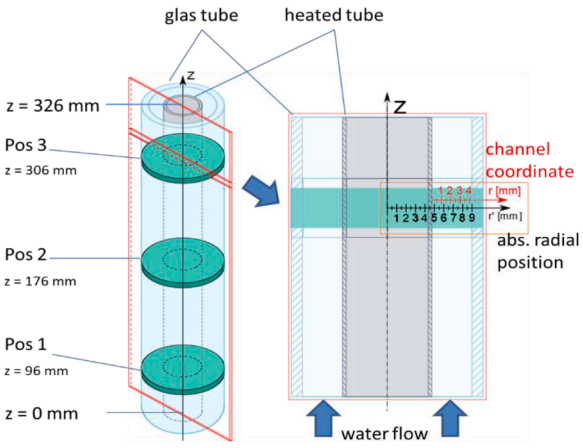

Fig. 4. Axial height positions for the measurements of the thermal hydraulic parameters.

$$\rho\frac{\partial\vec{u}}{\partial t}+\rho\{\nabla\cdot(\vec{u}\otimes\vec{u}) \quad \vec{u}(\nabla\cdot\vec{u})\}= \quad \nabla p + \nabla\cdot\{(\mu+\mu_t)(\nabla\vec{u}+(\nabla\vec{u})^T)\}+\vec{f} \tag{2}$$

$$\frac{\partial\phi}{\partial t}+\nabla\cdot(\phi\vec{u})= \quad \frac{1}{\rho_l}\dot{m} \tag{3}$$

$$C_p\left(\frac{\partial T}{\partial t}+\vec{u}\cdot\nabla T\right)=\nabla\cdot((\lambda+\lambda_t)\nabla T)+Q. \tag{4}$$

Equations (1)-(2) are the mass and momentum conservation equations, respectively, in which $\vec{u}$ (m/s) is the velocity vector, ρ (kg/m^3) the density, and the subscripts l and v denote the liquid and vapor phases, respectively; $\dot{m}$ (kg/m^3s) is the phase change rate (a positive value for vaporization, and a negative value for condensation); t (s) is the time, p (Pa) the pressure, μ $(Pa{\cdot}s)$ the dynamic molecular viscosity, μ_t $(Pa{\cdot}s)$ the turbulent eddy viscosity, and $\vec{f}$ (N/m^3) the body-force vector. Equation (3) is the governing equation for the color function f, which signifies the volume fraction of liquid inside a given control volume. The average density and viscosity within such a control volume (in this formulation a computational mesh/cell) are respectively defined as:

$$\rho=\phi\rho_l+(1 \quad \phi)\rho_v \text{ and } \mu=\phi\mu_l+(1 \quad \phi)\mu_v \tag{5}$$

The advection term in Eq. (3) is discretized according to the rational

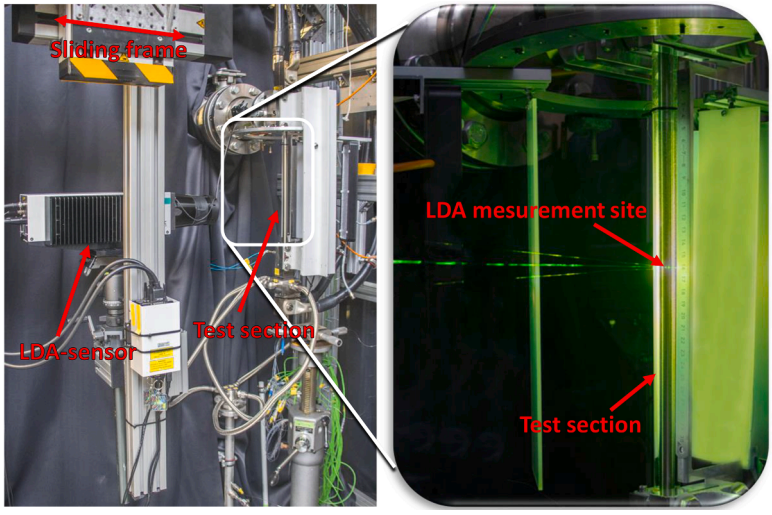

Fig. 5. LDA measurements applied at the annual gap test section (left) and a magnified view of the test section during a measurement.

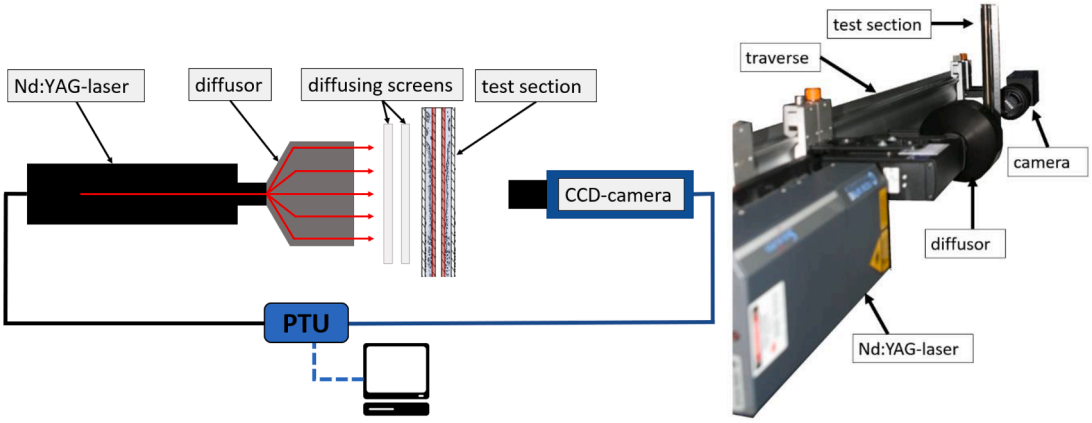

Fig. 6. Shadowgraphy measurement system for bubble size distribution.

CIP-CSL2 scheme (Nakamura et al., 2001; Xiao et al., 1996). To prevent smearing of the color function, an interface sharpening algorithm (Sato and Niceno, 2012) is employed. Equation (4) is the energy balance equation, in which $C_p (J/m^3K)$ is the specific heat at constant pressure, T (K) the temperature, λ (W/mK) the thermal conductivity, $\lambda_t (W/mK)$ the turbulent thermal conductivity, and $Q (W/m^3)$ the volumetric heat source. The turbulent thermal conductivity is calculated according to $Pr_t = (\mu_t/\rho)/(\lambda_t/C_p)$, where Pr_t (= 0.9) is the turbulent Prandtl number. Detailed derivations of Eqs. (1)-(4) are given in Appendices A and B of Sato and Niceno (2013).

Turbulence is modeled here using Large Eddy Simulation (LES), the Smagorinsky subgrid-scale model (Smagorinsky, 1963) being adopted to estimate the turbulent eddy viscosity μ_t. A Smagorinsky constant of $C_s = 0.17$, which is the theoretical value derived by Lilly (1967), has been employed in this study. Note that any interaction between the liquid turbulence and the liquid-vapor interface is not taken into account in the present formulation. On the right side of Eq. (2), the body-force vector $\vec{f}$ includes both gravity and surface tension forces. To take into account the effect of buoyancy, the Boussinesq approximation (Tritton, 1977) is introduced to the body force via the density difference between liquid and vapor. The surface tension coefficient is set to a constant value at the saturation temperature, meaning that the Marangoni effect (Burdon, 2014) is neglected in the simulations. Brackbill's Continuum Surface Force (CSF) model (Brackbill et al., 1992) is employed to represent the effects of surface-tension. In order to avoid strong parasitic currents being generated, we use the density-scaled form of the CSF model here (Brackbill et al., 1992).

The phase-change rate at the liquid-vapor interface is computed directly from the heat fluxes on the two sides. The temperature at the liquid-vapor interface is assumed to be the saturation temperature at the prevailing pressure, though away from the interface the conditions of superheated liquid and subcooled vapor are properly taken into account. The phase change rate $\dot{m}$ at the liquid-vapor interface is modeled as $\dot{m} = \frac{q_l + q_v}{L} \frac{S_{int}}{V}$, where q_l and q_v are the heat fluxes (W/m^2) derived from the liquid and the vapor sides of the interface, respectively; L (J/kg) is the latent heat of vaporization, S_{int} (m^2) the area of the liquid-vapor interface in the computational cell under consideration, and V (m^3) is the cell total volume. The area S_{int} is calculated by means of the marching cube algorithm (Lorensen and Cline, 1987), which has been proven successful for this type of flow (Sato and Niceno, 2013). The heat fluxes at the interface are defined as $q_l = (\lambda_l + \lambda_t)(\nabla T_l) \cdot \vec{n}$ and $q_v = (\lambda_v + \lambda_t)(\nabla T_v) \cdot \vec{n}$, where T_l and T_v are the temperatures in the liquid and vapor phases, respectively, $\vec{n}$ the unit normal vector to the interface, pointing from the vapor to the liquid phase. Note that the temperature defined in cells filled with liquid phase and the temperature at liquid-vapor interface are both used for the computation of ∇T_l, and the same is true for the vapor phase. More details of the sharp-interface phase-change model are reported in Sato and Niceno (2013).

3.2. Nucleation-site model and micro-layer model

The nucleation-site model originally proposed by Sato and Niceno (2017, 2018) is used in this work. The locations of the nucleation sites are prescribed *a priori* on the heat-transfer surface, together with a nucleation activation temperature T_{act}. Each nucleation site location is selected using a non-biased, random number generator in order to distribute the nucleation sites on the heat-transfer surface without examining the micro-scale imperfections of the surface. When the temperature at any nucleation site reaches T_{act}, a small vapor bubble (seed bubble) is placed at the site. The seed bubble is assumed to be initially hemi-spherical in shape, the radius being one cell width of the underlying grid. This of course means that the model is dependent on the grid spacing adopted, and a grid refinement study is then required to evaluate the influence of this assumption on the model predictions.

The nucleation activation temperature T_{act} is obtained from the available experimental data to model the active nucleation site density as a function of the measured wall temperature. In cases in which one needs to simulate nucleate boiling without recourse to experimental data, a correlation for the active Nucleation Site Density, NSD, for example those of Hibiki and Ishii (2003) or Kocamustafaogullari and Ishii (1983), may be used instead. In this study, the model proposed by the latter authors is used, because it specifically takes into account the flow rate and the degree of subcooling, thereby reducing the number of assumption.

The depletable micro-layer model used here includes the *wall-adhesion model* developed earlier by Sato and Niceno (2015). It has been shown that the model is a necessary addition to a cell-wise CFD simulation, and is required to resolve the phase-change phenomena taking place in the thin liquid film (micro-layer) beneath each growing bubble. If one were to incorporate the physics of the micro-layer directly into the CFD simulation, the disparity in cell size between the micro-layer and the bulk of the flow domain would render the calculation unfeasible. Hence, a micro-layer model of some description is a necessity. In the context of the depletable micro-layer model, the micro-layer thickness δ (m) is treated as a variable stored at the center of *wall-adjacent cells* (i.e. the fluid cells next to the wall), with the tacit assumption that the wall is coincident with a cell boundary. The thickness of the micro-layer decreases as a result of vaporization. In the micro-layer model of Sato and Niceno (2015), the initial micro-layer thickness δ_0 is defined as $\delta_0 = C_{slope}\, r_L$, where C_{slope} is constant, obtained either directly from measurement or via numerical experiments, and r_L (m) is the horizontal distance from the nucleation site to the cell center of the wall-adjacent cell containing the triple line, i.e. the line in which the liquid, vapor and solid phases jointly come into contact (on the scale of the CFD mesh). The linear modeling assumption, i.e. $\delta_0 = C_{slope}\, r_L$, is based on the observations of Utaka et al. (2013). For example, $C_{slope} = 4.46 \times 10^{-3}$ was deduced for water, and $C_{slope} = 1.02 \times 10^{-2}$ for ethanol, in each case relating to pool boiling from a heated quartz glass surface at atmospheric pressure; in addition, C_{slope} appears to be almost independent of the applied heat flux. In our model, we consider that C_{slope} depends on both the material and surface-roughness properties of the heat-transfer surface, as well as on the ambient pressure. Thus, when we simulate nucleate boiling with an unknown combination of working fluid, material properties, surface-roughness and pressure, we first perform a parameter study to determine C_{slope} in such a way that the bubble growth rate agrees with the corresponding measurement. In this study, we adopt the value $C_{slope} = 2.45 \times 10^{-2}$, which had been obtained for the simulations of Gaertner's pool boiling experiment (Gaertner, 1965), as described by Sato and Niceno (2018).

The effect of pressure on micro-layer formation has recently been measured by using interferometry for pool boiling (Wang et al., 2023) and convective boiling (Kossolapov, 2021) of water, and both the measurements showed that micro-layers are apparently formed up to system pressures of 3 bar. Note that Indium Tin Oxide (ITO) was used as the heat transfer surface in both the experiments, which is differ from Zircaloy-4 used in the COSMOS-L experiment, and thus the micro-layer formation, i.e. thickness and length, may also different especially because of the contact angle. Although the micro-layer formation on Zircaloy-4 is unknown, we used the micro-layer model in the CFD simulation because the COSMOS-L experiment presented in this paper was performed at the system pressure of 2 *bar*, which is lower than the threshold of 3 *bar*.

3.3. Discretization

The governing equations are discretized using a finite-volume approach. A staggered-variable arrangement (Harlow and Welch, 1965) is adopted, with the vector velocity and body-force components defined on cell faces, and the scalar variables pressure, temperature, color function and phase-change rate defined at cell centers. The projection method (Chorin, 1968) is used for the coupling between the

pressure and velocity fields. The spatial discretization is based on a second-order-accurate, upwind scheme for the advection terms, and a second-order, central-difference scheme for the diffusion terms. The time discretization is first-order implicit for the diffusion terms, and first-order explicit for the advection terms. A first-order scheme is employed for the time discretization, instead of a second-order scheme, such as that of Adams-Bashforth, (Ferziger and Perić, 2002). The time increment $\Delta t$is then limited both by the CFL condition (Courant et al., 1928) associated with the explicit time discretization of the advection term in Eq. (2), and by the surface tension treatment, also in Eq. (2). The details related to the time increment are described in Sato and Niceno (2018). It was found that no instability arises in the present calculations if a safety factor of 0.25 is applied to the CFL limit of Δt.

3.4. Computational domain and boundary conditions

Because the CFD code PSI-BOIL can only deal with an orthogonal Cartesian grid, the test section was modelled as a rectangular domain, as illustrated in Fig. 7 (right). This modification artificially decreases the ratio of the volume of the channel to the area of the heat-transfer surface by 30%, which may result in discrepancies between experimental measurements and CFD predictions. The computational domain is 356 × 29.7 × 4.82 mm^3in the axial, lateral and wall-normal directions, respectively, with 4608 × 384 × 72 cells in each coordinate directions (≈127 million cells in total). Twelve cells out of the 72 in the wall-normal direction are used to represent the solid heater. The cell size in the fluid domain is 77 μmin each direction.

The inlet/outlet boundaries are labeled in Fig. 7 (right). At the inlet, turbulent flow conditions are introduced by means of an anisotropic Gaussian random process (Li et al., 1994). The boundary conditions at the side of the computational domain are periodic. The outlet boundary conditions are of the Neumann type (i.e. zero gradient) for the velocity, pressure and temperature fields. As mentioned earlier, the locations of the nucleation sites are chosen using a non-biased, random number generator in the same way as for the pool boiling simulations performed earlier (Sato and Niceno, 2017, 2018).

3.5. Parametric study for nucleation site density, NSD, modelling

The nucleation site density model proposed by Kocamustafaogullari and Ishii (1983) is employed in this study because it can take into account the influence of flow rate and degree of subcooling on nucleation site density. However, the model does not have parameter for e.g., surface roughness, which has impact on nucleation site density. Thus, we used the contact angle θ as a *tuning parameter* to take into account the unmodelled influence (e.g. surface roughness) in such a way to fit the calculated temperature to the measurement. Three cases of contact angle at 27.5°, 55° and 110° have been evaluated. The computed NSD is shown in Fig. 8, and compared with those obtained from the Lemmert-Chawla model (Lemmert and Chawla, 1977).

Three simulation cases were computed, each with an applied wall heat flux of 736 kW/m^2. The computational cells are uniform cubes of 116 μm for the fluid domain and uniform rectangular of thickness 71 μm for the solid domain in each case, which corresponds to the Medium grid used for the grid dependence study in the following section. The computed wall temperature profiles are compared with measured data from the COSMOS-L facility in Fig. 9. Here, the computed wall temperature is the averaged value in the lateral direction at the given height. As the contact angle decreases, the wall temperature increases, which is considered to be reasonable, since NSD is smaller for lower contact angle. The case with a contact angle of 27.5° is closest to the measurement. Consequently, we adopt $\theta = 27.5°$ for the numerical simulations described in the following sections.

3.6. Grid dependency study

A grid dependency study has been performed for the three cases with different cell sizes, as listed in Table 1. The directions of Z, Y and r are, respectively, the axial, lateral and normal-to-wall directions depicted in Fig. 7. The applied heat flux was set at 596 kW/m^2, and the contact angle used for the NSD model was set to 27.5°, for the reasons given in Section 3.5. The computations were continued until the wall temperature reached a pseudo-steady condition. The evolution of the temperature field for the Fine Grid simulation is shown in Fig. 10. The temperatures displayed in the figure correspond to the locations of the thermocouples in the test section (Fig. 4). In each case, the value is the average temperature in the Y-direction at the given height. The Fine Grid simulation ran for around two months using 512 cores on the supercomputer at CSCS, which uses Intel® Xeon® E5-2695 v4 @ 2.10GHz as CPUs.

The computed profiles for the wall superheat are compared in Fig. 11 with the measured data. Note that two measured data points exist for each height because two thermocouples were employed, which indicates the uncertainty of temperature with respect to the circumferential position, and general lack of axial symmetry of the flow. As the grid is made finer, higher wall temperatures are predicted. The calculated temperatures display large grid dependency at the lower location,

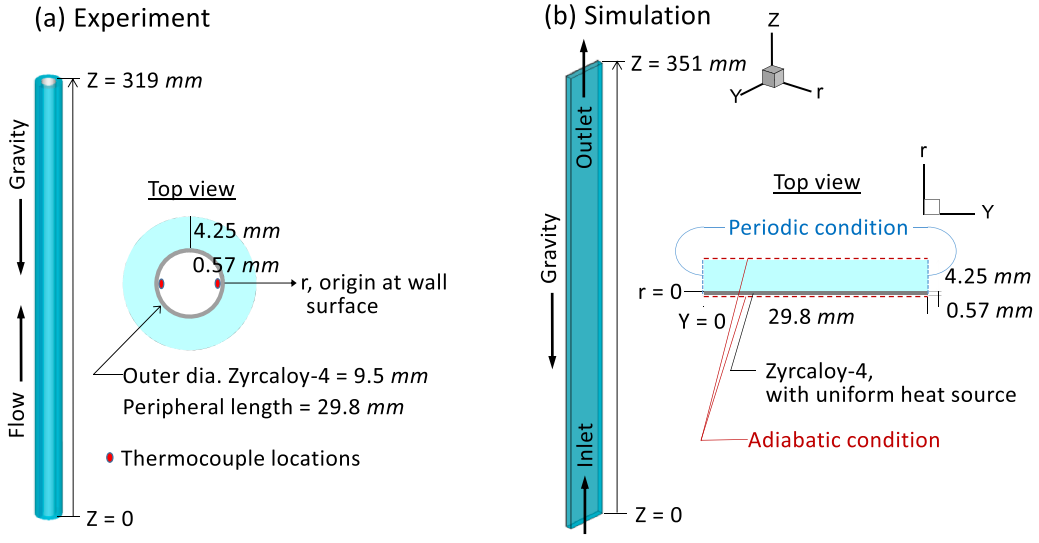

Fig. 7. Schematics of (a) the experimental set-up and (b) the computational domain and boundary conditions.

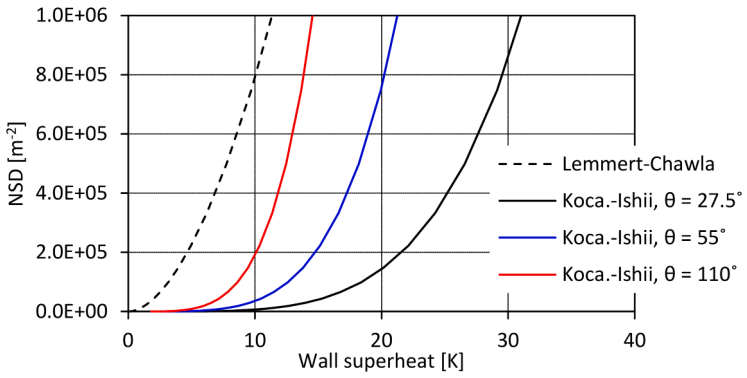

Fig. 8. Comparison of Nucleation Site Density, NSD, as the function of wall superheat between the models of Lemmert-Chawla and the Kocamustafaogullari-Ishii at 2 *bar* pressure and a mass flow rate 400 kg/m^{2}s with contact angles at 27.5°, 55° and 110°, respectively.

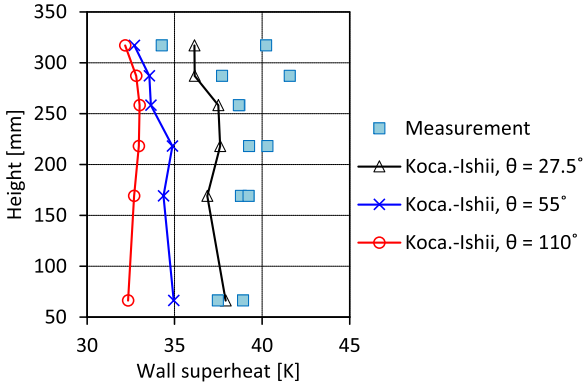

Fig. 9. Comparison of the wall superheat profiles between the measurement at COSMOS-L and the CFD simulations with different contact angles in the Kocamustafaogullari-Ishi model.

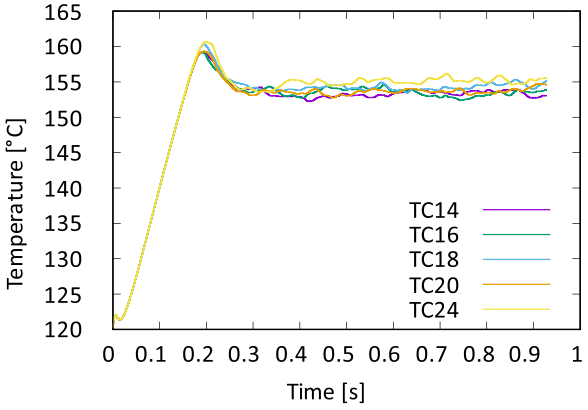

Fig. 10. Computed time-history of wall temperature at the locations corresponding to the thermocouples for the Fine grid simulation.

Table 1
Computational grid for the grid dependency study.

Grid name	Cell size (μm)		Number of cells			Total number of cells
	fluid domain	solid domain	X	Y	r	
Coaese	Cube of 155	155 × 155 × 95	2304	192	36	15′925′248
Medium	Cube of 116	116 × 116 × 71	3072	256	48	37′748′736
Fine	Cube of 78	78 × 78 × 48	4608	384	72	127′401′984

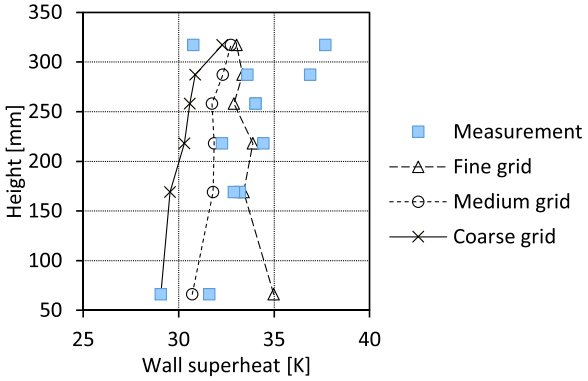

Fig. 11. Comparisons of vertical temperature profiles between measurement and simulation for different sizes of grid.

that between the Coarse and Fine simulations being 6 *K* at the lowest point. This result indicates that the solution still depends on the grid size, especially at the lower position, even if the Fine Grid option is employed. Ideally, we should use still finer grids to evaluate further the grid dependency effect. However, the computational resources we can currently access are too limited to allow such a study to be undertaken at this time. Thus, we use the results from the Fine Grid simulations in the following analysis.

4. Results of experiment and simulation

In the experiment, DNB-type CHF was measured for an applied heat flux of 1.23 MW/m^2 in the case of $T_{in} = 80°C$, $G = 400\ kg/m^2s$ at 2 *bar*. The criterion for DNB was defined to appear spontaneously at a specific applied heat during the pseudo-steady-state measuring procedure. Then a strong local temperature increase of about 200 *K/s* could be observed. Therefore, a maximum heater temperature was selected as a switch-off criterion, the local exceeding of which is considered as a DNB event. Unfortunately, this criterion is in opposition to requirements to conduct measurements of bubble velocity, flow and bubble distributions. While the detection of the spontaneously occurring, CHF requires the shortest possible reaction time, in combination with a fast power shut-off, the measurements of the averaged bubble velocity, flow observations and the bubble size distribution require a certain minimum time in excess of this. On reaching DNB, the electrical heating must be shut off immediately to avoid damage to the heater. In contrast, estimation of the averaged bubble velocity and bubble size distributions involves a continuous observation of these parameters for some duration in order to avoid overemphasis of singular events.

Therefore, reduced heat flux levels needed to be chosen to investigate the wall temperatures, flow velocities and bubble size distributions at steady-state conditions. In the studies relating to this paper, the focus lies on comparison of the experimental and numerical data at a heat flux corresponding to 50% of the CHF level. At this reduced level, coalescence phenomena associated with DNB, and hence CHF, are not strongly pronounced. Thus, the focus here can be set on bubble generation and recondensation without additionally facing the challenging task of modelling bubble coalescence phenomena. Hence, we concentrate on the two vertical measurement positions 1 and 2 (Fig. 4), located at the beginning and the middle of the test section, at which coalescence is almost negligible.

4.1. Flow observations

During the experiments, numerous images of the flow were taken using standard and high-speed cameras. The videos are provided as supplementary information:

- Video 1[2] for the standard camera, and
- Video 2[3] for the high-speed cameras.

Visual observation of the flow gives an insight into bubble formation, bubble lift-off and interaction, as well as of condensation. Selected images from Video 1 and Video 2 are shown in Fig. 12 and Fig. 13, respectively. The first video (snapshots in Fig. 12) shows the upper part of the test section for various applied heat fluxes and permits a global view of the flow and evolution of the relevant flow structures to be attained. Beginning at a heat flux at 40% of the CHF-value, the images from the video clearly show the increasingly dynamic nature of the flow. As can be seen, bubble growth and bubble condensation phenomena occurring very rapidly.

Fig. 13 shows the boiling flow at a heat flux corresponding to 50% of CHF at three discrete positions, Pos 1-3, which represents flow is the focus of the present work. The selected images provide representative insights into the growth and condensation of the steam fraction. However, an important observation from the video obtained from of the high-speed cameras (Video 2) is that the rates of bubble growth and condensation are not constant/steady in time, and a periodic pulsation phenomenon is clearly evident. Unfortunately, for positions 1 and 2, individual images cannot be evaluated from the high-speed video for quality reasons, so the time spans of the pulsation could not be considered exactly. Nevertheless, the images give a good overall impression of the flow conditions, and show that the relevance of coalescence phenomena at this lower heat flux are almost negligible compared to those after critical power. This is a consequence of the low void fraction, meaning that the bubbles rarely approach each other and coalesce. Overall, the videos thus indicate the dynamic character of the flow, with the processes of bubble growth and bubble condensation occurring very rapidly.

A comparison of the bubble shapes observed in the between experiment and predicted from the simulation is given in Fig. 14. From the experimental findings, only the bubbles on a sliced plane through the annulus have been visualized. The computed bubble shapes and temperature distribution refer to a snapshot taken at $t = 0.8\ s$, when pseudo-steady-state conditions have been achieved for the wall temperature, see Fig. 10. As an overall trend, the experimental and the simulation data display optically good agreement; e.g. the number of bubbles and bubble sizes increase in the downstream region. More quantitative comparisons of the bubble shapes and sizes are given in the following sections. The computed temperature on the heat-transfer surface T_{wall} is also visualized in Fig. 14. The wall temperature T_{wall} is low at the inlet (80℃), but increases rapidly because of the inefficiency of single-phase heat transfer. Then, in the downstream of single-phase flow, nucleation sites are activated due to the high wall temperature. The highest temperature (≈160℃) is observed in the zone where the nucleation sites are not yet activated. Downstream of the highest temperature region, the wall temperature decreases due to the bubble nucleation and sliding bubbles on the wall.

Fig. 15 gives a magnified view of the region around Pos 2 at $t = 0.80\ s$ and $t = 0.81\ s$, in which streaks of high wall temperature are observed downstream of a bubble. By comparing T_w at different times, one can notice that the high wall temperature streak disappears, as the bubble slides over it, as indicated by the black dashed-line circle in the figure.

4.2. Wall superheat

Comparisons of the wall temperatures between the measurement and simulation are given in Fig. 16. To detect trends in the temperature, for illustration purposes, we have also included the cases with applied heat fluxes of 30% and 80% of CHF. In general, the simulation results agree well with measurement. In the case of an applied heat flux 80% of CHF, the temperature decreases with height in the region above 250 *mm* according to the simulation, which agrees well with the measurement data. The decrease in wall temperature downstream can be explained by the increase of the mean flow velocity resulting from the total volume expansion associated with boiling.

The good agreement of the wall superheat between measurement and simulation implies that the local heat transfer at the wall, which comprises multiple heat transfer mechanisms resulting from single-phase liquid, sliding of bubbles along the wall, evaporation and quenching, have all been computed appropriately in the CFD simulations.

4.3. Void fraction

The computed void fraction at Pos 1-3 are shown in Fig. 17 (left), representing time- and space-averaged values, $\overline{\overline{\alpha(r)}}$. The time-averaging has been performed from 0.6 *s* to 0.9 *s*, and the space averaging performed in the Y-direction at the specific elevation and radial position. Specifically,

$$\overline{\overline{\alpha(r)}} = \frac{1}{t_1 \quad t_0} \frac{1}{Y_1 \quad Y_0} \int_{t_0}^{t_1} \int_{Y_0}^{Y_1} \alpha(Y, r, t) dY dt, \tag{6}$$

where $(t_0, t_1) = (0.6, 0.9)\ s$, and $(Y_0, Y_1) = (0, 29.8)\ mm$; see Fig. 7 (b) for the definition of Y.

The RMS of the void fraction is shown in Fig. 17 (right). As can be seen, the RMS value is larger than the average value, which indicates that there are large fluctuations of void fraction both in space and time.

The time-averaged void fraction in the sliced plane $Y_2 = 19.6\ mm$, $\overline{\alpha(Y_2, r)}$, at the elevations corresponding to Pos 1-3 are shown in Fig. 18 (left), as representative Y-positions. The time-averaged value is defined as:

$$\overline{\alpha(Y_2, r)} = \frac{1}{t_1 \quad t_0} \int_{t_0}^{t_1} \alpha(Y_2, r, t) dt. \tag{7}$$

A sharp peak is observed for Pos 3 at $r = 0.4\ mm$, which is considered to be caused by the existence of a nucleation site upstream of this location. The RMS value in the same sliced plane is given in Fig. 18 (right).

4.4. Bubble velocity

Measurements of bubble velocity were made at each of the three vertical measurement positions (Pos 1-3 in Fig. 4) in the axial and radial

[2] https://publikationen.bibliothek.kit.edu/1000126774.
[3] https://publikationen.bibliothek.kit.edu/1000126559.

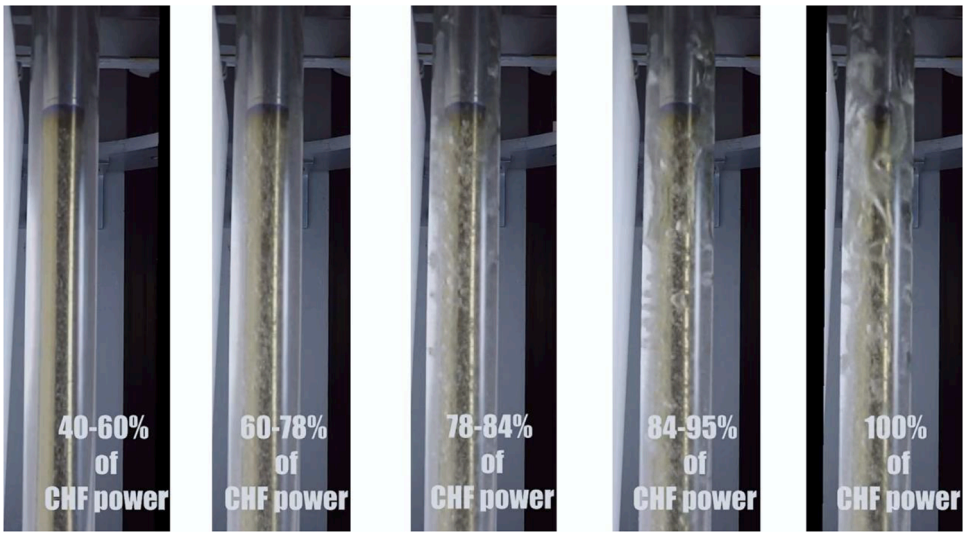

Fig. 12. Snapshots of the boiling flow recorded with the standard camera (Video 1) for different applied heat-flux.

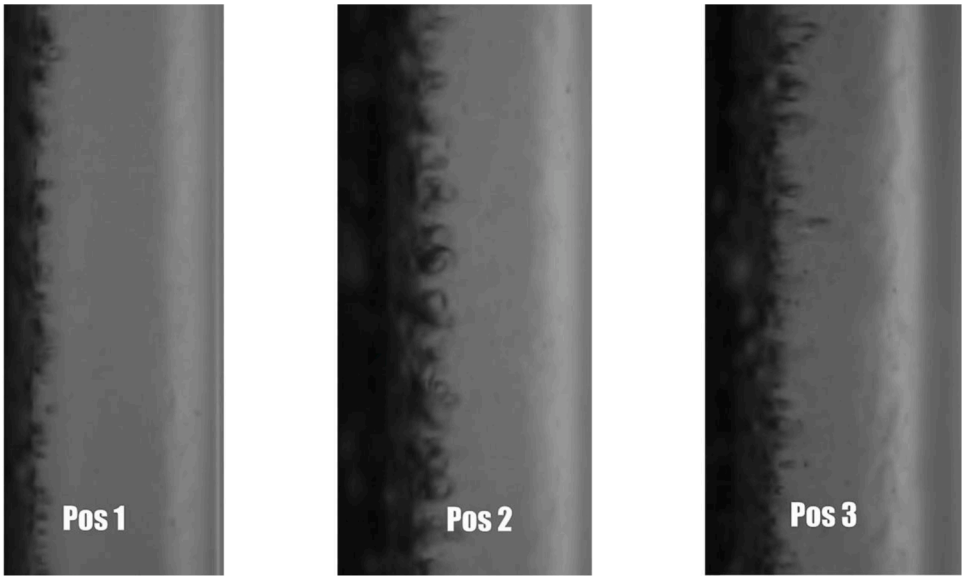

Fig. 13. Detailed image of the flow at the three measuring positions with short exposure time recorded with the high-speed camera (Video 2).

directions over the entire annular gap. These measurements were repeated at least three times for every parameter set, so that enough detected bubbles were available for a statistical evaluation. Fig. 19 shows the measured, time-averaged bubble velocities of the axial and radial components in the experiment. The error bars in this figure represent the deviations of the individual measurements.

During the vertical ascent through the annular gap, the bubbles theoretically experience an acceleration due to (i) their buoyancy and (ii) acceleration of the liquid phase. Here, the buoyancy force contributes to the difference of upward velocities between the bubble and liquid phase, while the acceleration of the liquid phase is caused by the increase of the vapor fraction. However, the measured upward bubble velocity did not show an acceleration with the ascent, as shown in Fig. 19 (left). We discuss the reason for this here.

The liquid-phase velocity field was not specifically measured in the experiment, but the upward current velocity of the liquid phase has estimated to be slightly lower than that of the bubbles due to buoyancy of bubbles. By considering the Richardson number, the influence of the buoyancy force can be quantified:

$$Ri = \frac{\rho_l \quad \rho_v}{\rho_l} \frac{d_H g}{w^2} = \frac{Gr}{Re^2}, \tag{8}$$

where d_H is the hydraulic diameter, Gr the Grashof number, and Re the Reynolds number. The Richardson number provides a measure of the strength of the buoyancy force to that of the shear flow force. For values $Ri << 1$, the buoyancy force can be neglected. For the present application, $Ri = 0.14$, so that buoyancy terms are considered non-influential, resulting in a constant difference between the bubble and upward liquid velocities throughout the vertical annulus. Note that this assumption is only valid if bubble coalescence is negligible, and the bubbles remain small. Consequently, the similar upward velocity profiles at Pos 1-3 are considered to be caused by (i) non-influential buoyancy force owing to $Ri << 1$, and (ii) the non-significant acceleration of the liquid phase along the ascent; i.e. no increase of vapor fraction because of subcooling of liquid in the bulk region.

It must be pointed out that the measurement uncertainty of bubble velocity in the outer region of $r > 3.5\ mm$ is higher than that in the inner region, due to the reflection of the laser at the glass tube. Especially, $\overline{w}$ of

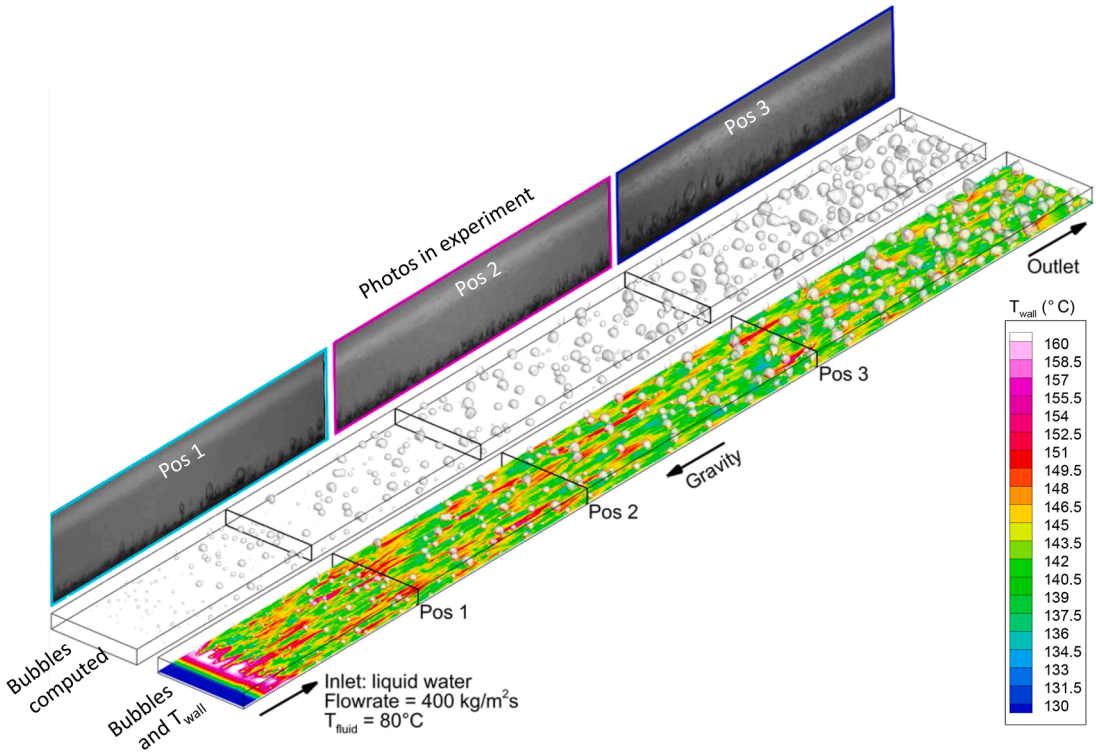

Fig. 14. Comparison of the bubble shapes between experiment and simulation. The experimental images were obtained using high-speed video cameras located at Pos 1-3 defined in Fig. 4.

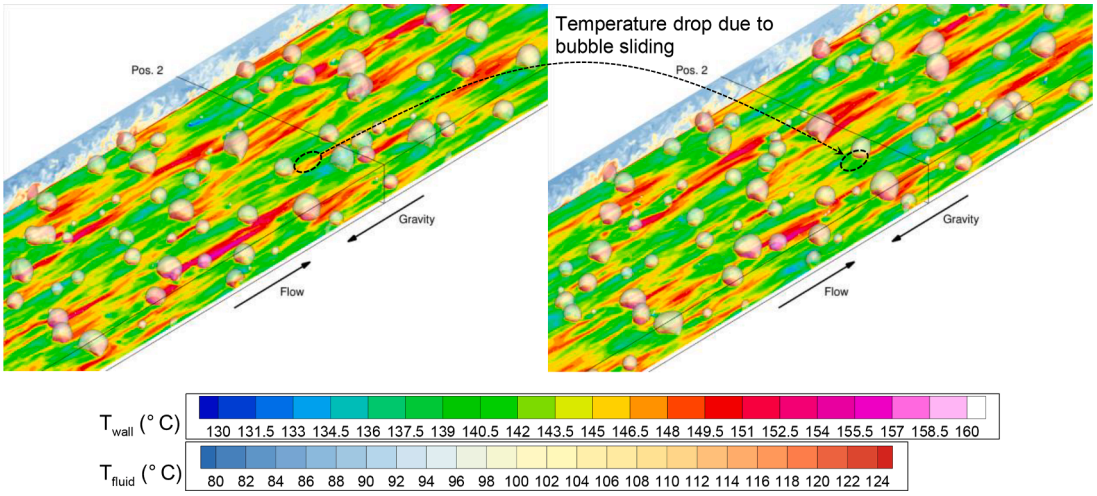

Fig. 15. Computed flow field around Pos 2 at t 0.80 s (left) and t 0.81 s (right).

Pos 3 in the range $r > 3.5$ mm is lower than that of Pos 1 and 2; Fig. 19 (left), which was classified as valid by the measuring system, but considered to be affected by the measurement uncertainty. Additionally, the probe size of the LDA measurement was chosen to be 0.7 mm, so that only bubbles smaller than this were taken into account.

Considering the velocity boundary layer on the heated surface, one can notice that the boundary layer thickness increases downstream, see Fig. 19 (left). The boundary layer is thickened by the radial velocity near heated wall, as shown in Fig. 19 (right), which results from the bubble growth, and lift off process.

The numerical simulation also indicates an influence of bubble formation at the heated rod on the velocity distribution. Fig. 20 shows time and space-averaged results of the axial and radial velocities. The averaging in space is taken over the entire circumferential direction for each vertical position; the time-averaging is performed from 0.6 s to 0.9 s. The velocity profiles are not smooth in the far field, away from the heat-transfer surface, because there are insufficient bubbles in this region. The peak in the axial vapor velocity profile appears around r = 0.8 ~ 1.1 mm, where the void fraction reaches its maximum, as seen in Fig. 17 (left). The peak observed in Fig. 20 (left) increases in the upward/downstream direction; i.e. the peak at Pos 3 is greater than that at Pos 1. Since the axial vapor velocity is accelerated by the buoyancy force acting on the bubble, this result is considered to be reasonable. However, these features are not seen in the experiment. The peak in the radial velocity profile, Fig. 20 (right), is around 0.2 m/s, and appears in the vicinity of the heat-transfer surface. Compared to the measurement result Fig. 19 (right) the peak near the wall is similar, but the radial velocity in the region away from the wall is markedly different.

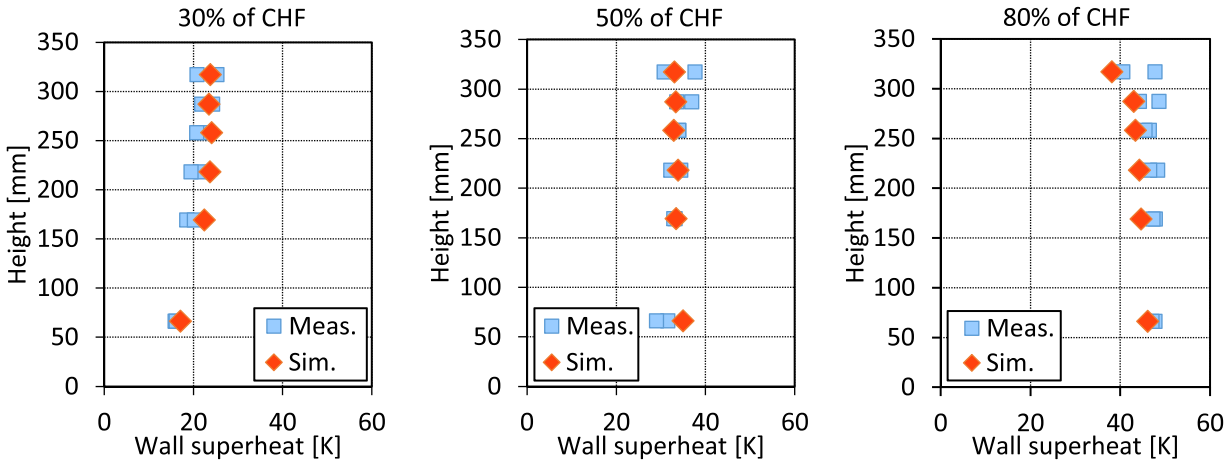

Fig. 16. Comparison of wall temperatures between measurement and calculation for an applied heat flux at 30% (left), 50% (middle) and 80% (right) of CHF.

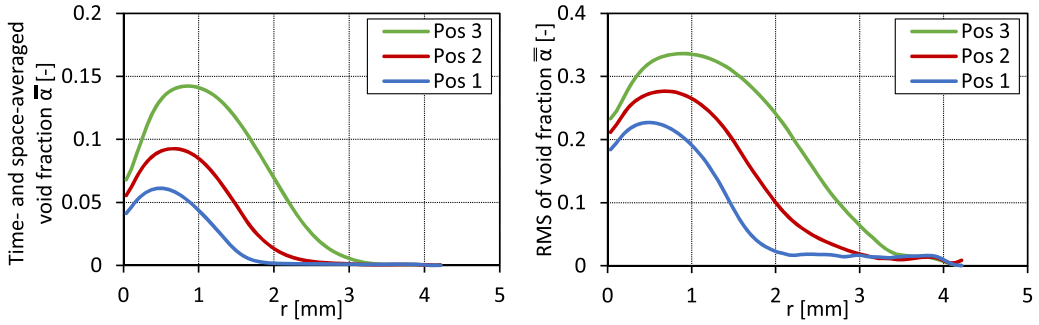

Fig. 17. Computed time- and space-averaged void fraction $\overline{\overline{\alpha(r)}}$ at Pos 1-3 (left) and its RMS value (right).

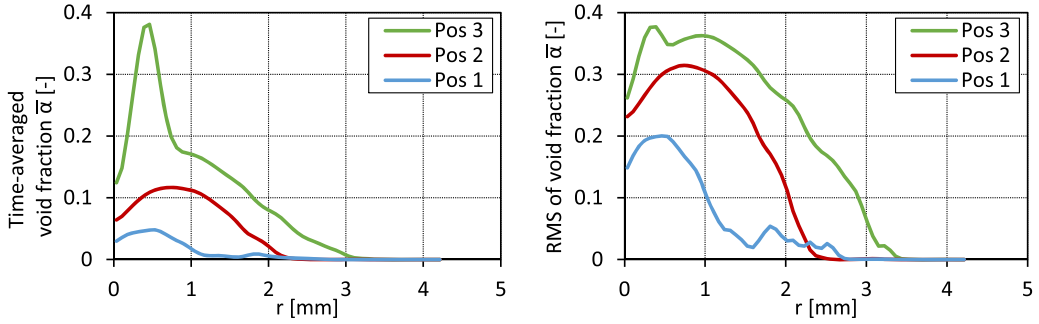

Fig. 18. Computed time-averaged void fraction in the plane Y_2 19.6 *mm* $\overline{\alpha(Y_2, r)}$ at the elevation of Pos 1-3 (left) and its RMS value (right).

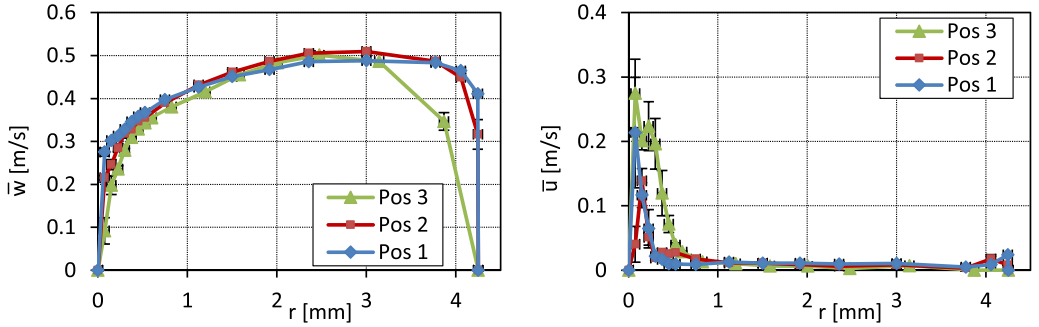

Fig. 19. Measured, time-averaged bubble velocity profiles in the annular gap for the axial and radial components at different vertical positions for boundary condition for 50% applied CHF power.

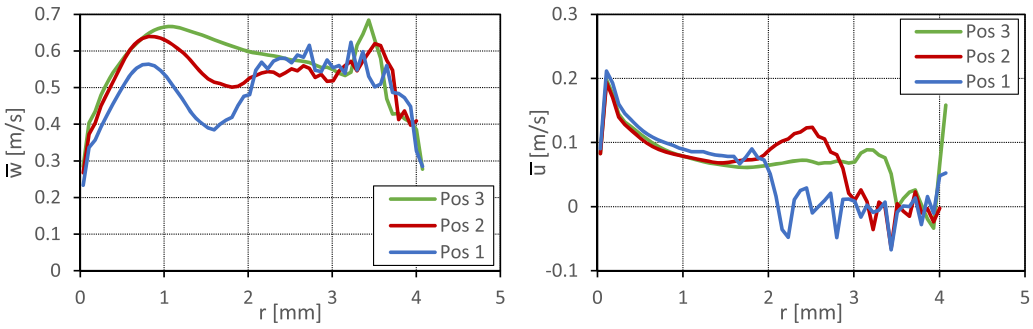

Fig. 20. Computed velocity profiles of vapor, averaged in space and time.

According to the measurement, the radial velocity asymptotes to zero for $r > 0.5\ mm$ (Fig. 19 (right)). The discrepancy between the measurement (Fig. 19) and numerical prediction (Fig. 20) is considered to be principally caused from underestimation of the condensation rate in the CFD simulation, as a result of using too coarse a mesh. The bubbles generated at the heat-transfer surface did not condense sufficiently, which led an increased in the radial velocity, which subsequently remained positive in the far field ($0.5\ mm < r < 2\ mm$); see Fig. 20 (right).

The computed velocity profiles of the liquid phase are shown in Fig. 21; these were not measured in the experiment. The axial velocity profile at Pos 1 is symmetric, because of the rectangular computational domain, but the higher velocity region moves toward the heat-transfer surface at upper elevations, due to the influence of the increased axial velocity of the bubbles in this region, and their induced drag on the liquid phase. The radial velocity in the liquid phase is much smaller, and almost zero for $r > 3\ mm$ at all elevations.

What is remarkable regarding the experimental results is the continuously increasing RMS value of the vertical bubble velocity in the downstream direction, as shown in Fig. 22 (left). The axial component of the RMS velocity, w_{RMS}, at the highest position is identical to the value of the averaged vertical velocity, as seen in Fig. 19. This is a consequence of the observed strong pulsations in the flow. The radial RMS velocities, u_{RMS}, for the lower two positions are much larger than that at the highest position, and indeed much larger than w_{RMS} values. However, the width of influence is largest for the highest position, Pos 3, and this extends over almost the entire annular gap.

The calculated RMS values of the bubble velocities are shown in Fig. 23. The values in the far field ($r > 2.5\ mm$) fluctuate because there are insufficient bubbles representing the vapor phase for a statistical average to be meaningful. The RMS predictions for the axial velocity are similar between Pos 1-3, and the value at Pos 3 resembles the experiment (Fig. 22 left): the peak w_{RMS} is $0.4\ m/s$, located near the heat-transfer surface, and decreases to half that value at $r = 0.5\ mm$. From the simulation, the RMS for the radial velocity is generally smaller than that measured, which is considered to be also due to the underestimation of condensation by too coarse a mesh being employed.

One of the major differences between the numerical and experimental data lies in the definition of the geometry. Whereas the experiments were conducted in a cylindrical annular gap, the numerical study was undertaken in a rectangular geometry (Fig. 7). This limitation of the CFD model has an impact on the behavior of the rising bubbles. In Fig. 24, the theoretically available space for growing bubbles in the two geometries is visualized. In this figure, the shaded region indicates the available space for the bubble cavities when they have reached their maximum size, and start touching each other. For the detachment process, the available space for the annular gap in the experiments is expanding, whereas the space available in the numerical set-up stays constant, as visualized in Fig. 24 (left). This mismatch also results in a difference in the pressure distribution across the channel. The differences in pressure could have an additional accelerating effect on the bubbles towards the outer glass tube in the experiment, though this has not been specifically investigated.

4.5. *Bubble size distribution*

The bubble size has an influence on the velocity and temperature fields, and is one of the key factors in accurately predicting the total heat and mass transfer rates. Fig. 25 (left) gives the distribution of the bubble diameters measured at Pos 1 and Pos 2. Almost 90% of the bubbles are in the range 0-200 μm, and bubbles of diameter larger than 400 μm have a relative frequency below 6%. Bubbles larger than 700 μm in diameter can be found only at the Pos 2. The bubble size distribution is similar for the two positions, since the bubbles collapse quickly after detachment from the heated surface, and do not flow downstream, a feature which could also be observed in Video 1.

Fig. 25 (right) shows the computed distributions. Again, a bubble diameter of 0-200 μm represents about 90% of the total. However, the bubble size distribution above 300 μm diameter displays a different tendency. From the measurements, the relative frequency of the appearance of such bubbles gradually decreases as the bubble diameter increases. In contrast, according to the simulation, bubbles of diameter 300-700 μm are absent entirely, and those larger than 1000 μm are observed instead. The aberration is considered to be caused by numerical error, the so-called spurious numerical bubble coalescence

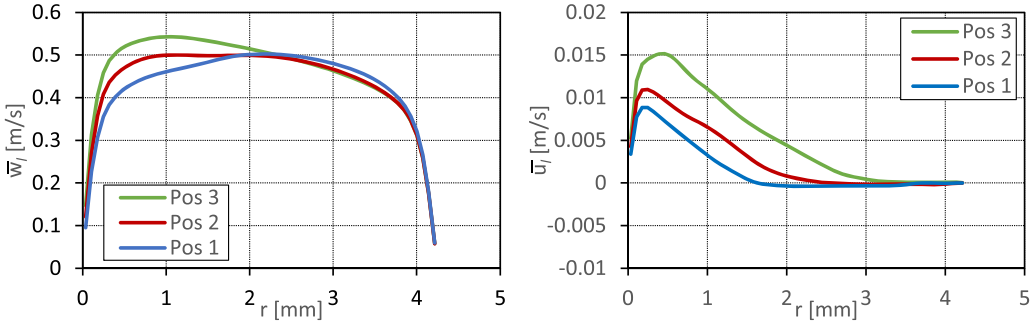

Fig. 21. Computed velocity profiles of the liquid phase averaged in space and time.

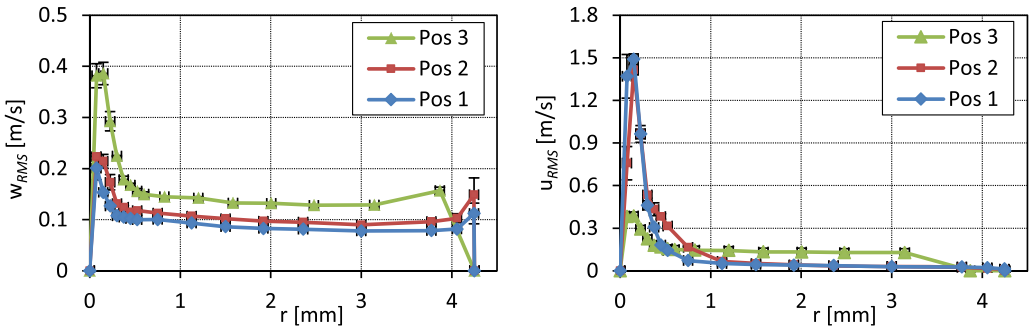

Fig. 22. RMS values corresponding to the averaged velocity profiles of Fig. 19.

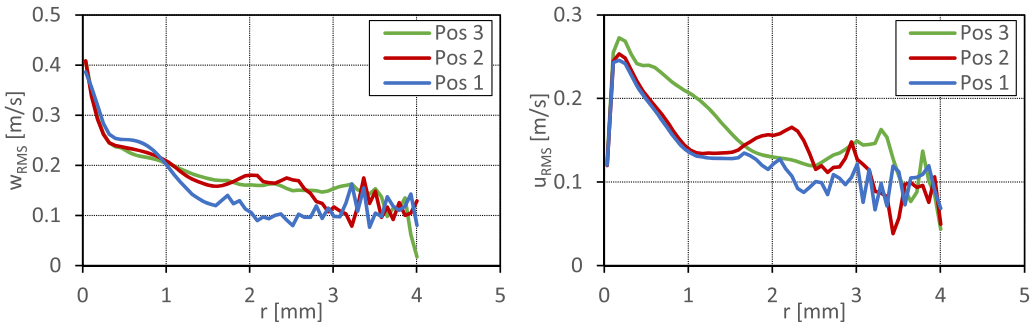

Fig. 23. Computed RMS of the vapor velocity, averaged over space and time.

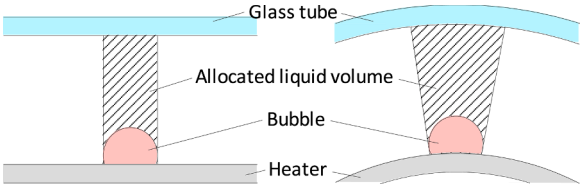

Fig. 24. Differences in geometry between the numerical (left) and experimental (right) studies.

phenomenon (Coyajee and Boersma, 2009). When the distance of the interfaces between two separate bubbles becomes narrower than one computational grid size, the bubbles are automatically merged in the simulation. To avoid this artificial numerical bubble coalescence, a more sophisticated model, e.g. a multiple marker formulation (Cifani et al., 2018; Kwakkel et al., 2013) must be used. This extension of the model is here postponed to a future work. Once a larger bubble is generated artificially, then it condenses more slowly than the smaller bubbles, because of the reduced interfacial area density. As a result, sliding of large bubbles along the heated surface is predicted in the simulation, as indicated in Fig. 15, but not observed in the experiment.

It is of interest to investigate the bubble size distribution in the radial direction at the different elevations from the viewpoint of the bubble dynamics as influenced by the overall liquid-vapor mass transfer. Fig. 26 compares experiment (left) and simulation (right) in this regard. Both figures reveal that the larger bubbles appear mainly in the vicinity of the heat-transfer surface, whereas the smaller bubbles, i.e. those of diameters less than 200 μm, are present across the entire width of the annulus. The differences in bubble size distribution between Pos 1 and Pos 2 are marginal for both the experiment and simulation. The measured bubble size distribution shows the presence of larger bubbles ($dia. > 500\ \mu m$) near the heated surface, i.e. at $r \approx 0.5\ mm$. With increasing distance from the heated surface, the bubble diameters continuously decrease, and from $r = 1.0\ mm$ outwards only small bubbles, i.e. with diameters below 200 μm, are present in the flow.

According to the computation, Fig. 26 (right), most of the larger bubbles lie along the line $dia. = 2r$, and the smaller ones slightly above

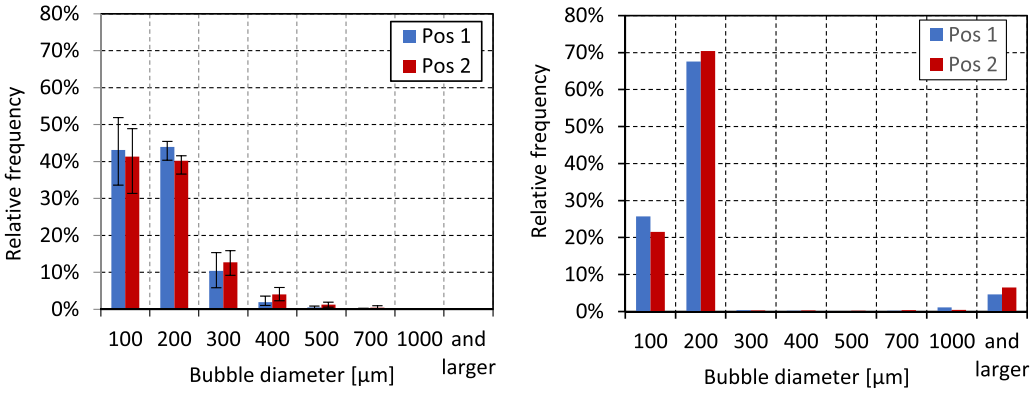

Fig. 25. Bubble size distribution measured (left) and computed (right) for an applied heat-flux of 50% CHF.

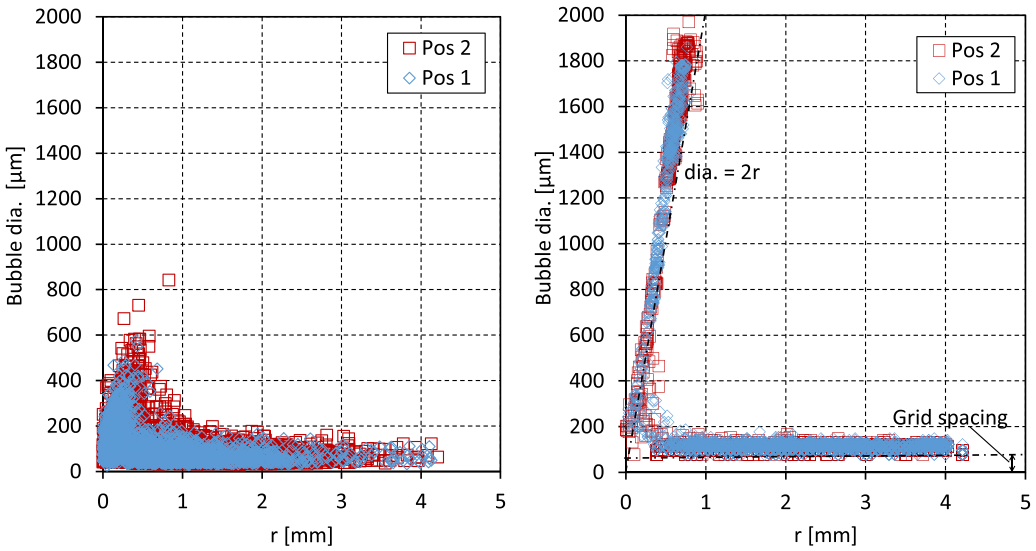

Fig. 26. Bubble diameter distribution as a function of radial position, measured (left) and computed (right), for an applied heat-flux of 50% CHF.

the line *dia.* = *grid spacing* (= 76 μm). A bubble with *dia.* = 2*r* represents a spherical bubble attached to, or sliding along, the heat transfer surface. The bubbles clustered around the line *dia.* = 2*r* are considered to be an artifact of the spurious bubble coalescence alluded to earlier. The computed bubbles slightly above the line *dia.* = *grid spacing* may indicate the capability of the interface tracking method to predict the bubble dynamics in the low-void regions, since the measurements reflect similar behavior.

4.6. *Bubble liftoff without sliding motion*

In this section, we consider the mechanisms of bubble liftoff without sliding motion, as was observed in the experiment. Fig. 27 illustrates a typical evolution of a seed bubble, as observed in the experiment with a temporal resolution of 3000 *fps*. The bubble then is first nucleated between the timeframe (1) and (2) in Fig. 27, and grows on the wall during timeframes (2)-(3). The bubble lifts off at timeframe (4), any sliding of the bubble along the wall not being observed. The bubble moves to the bulk region and condensates, as shown in the timeframes (5)-(6). The bubble shape is elongated in the wall normal direction, as seen in timeframe (6).

Qualitatively, similar bubble motion is predicted from the simulation, as evidenced in Fig. 28, in which the liquid-vapor interface and the temperature distribution are visualized at a frequency of 6000 *fps*. It is to be noted that not all the bubbles lift off without sliding, as shown in this figure, but many slide along the wall without lift off, as displayed in Fig. 15, and can also be seen in Video 1 of the experiment. Since the distribution in a sliced plane is drawn in this figure, only a few bubbles are to be seen. In contrast, multiple bubbles are observed in the experiment (Fig. 27), as a result of the perspective view. The evolutions of the mass-transfer rate distribution and bubble shape are displayed in Fig. 29, the location being the same as in Fig. 28.

In Fig. 28 (1), the nucleation site has been activated because the temperature at the site attained the activation temperature of 135.2*C*. Note that the locations of the sites are prescribed in the simulation, randomly distributed on the heat-transfer surface, with each site having a specific activation temperature. The bubble grows, and the temperature of the solid wall beneath the bubble decreases, as seen in Fig. 28 (1)-(3). The temperature drop in the solid around the nucleation site reflect the energy expended through mass transfer (latent heat of evaporation), as observed in Fig. 29 (1)-(3). The bubble shape at time (1) is squat, as a consequence of the micro-layer modelling, the bubble diameter on the wall reaching a maximum at image (2). Then, the bubble continues to grow in the wall normal direction, as shown in (3)-(4). During this period, vaporization takes place at the bottom of bubble and concurrently condensation occurs at the top, see Fig. 29 (3)-(4). In the situation seen in Fig. 29 (5), the rate of vaporization at the base of the bubble decreases, and the vapor condenses at the top, which "pulls" the bubble away from the wall. The computed bubble shape in Fig. 28 (5), i.e. elongated in the wall normal direction, is very similar to that observed in the experiment, Fig. 27 (6). From these observations, one can conclude that the bubble does not slide along the wall, but lifts off immediately following bubble growth, due to the condensation at the upper surface of the bubble in the subcooled flow stream.

The bubble dynamics during subcooled, forced-convection nucleate boiling, i.e. bubble growth, sliding, lift-off and collapse, is significantly influenced by the degree of subcooling in the bulk flow. In the case that the degree of subcooling is large, i.e. $T_{sub} > 55\ K$ for water at atmospheric pressure (Gunther, 1950), bubbles grow and collapse while they are still attached to the heated surface, without sliding or lifting off. In contrast, in the case of saturated boiling, bubbles grow, slide and then lift off; observations of this phenomenon, using high-resolution measurement techniques, were reported, for example by Klausner et al. (1993) and Maity (2000). The experiment of forced convection nucleate boiling flow in a vertical channel performed by Maity (2000) at saturation conditions has been simulated by Li and Dhir (2007) and Sato

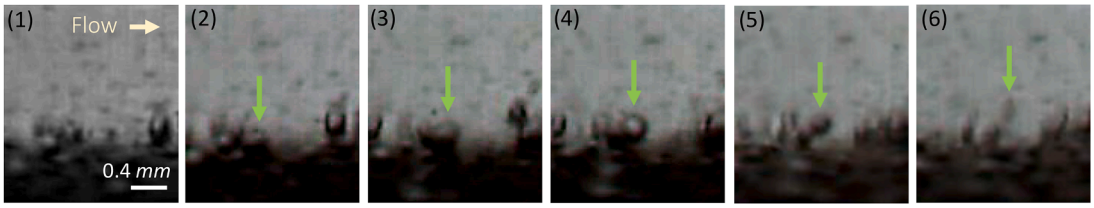

Fig. 27. Evolution of bubble growth and lift-off recorded by the high-speed video camera at Pos 3, visualized at 3000 *fps*.

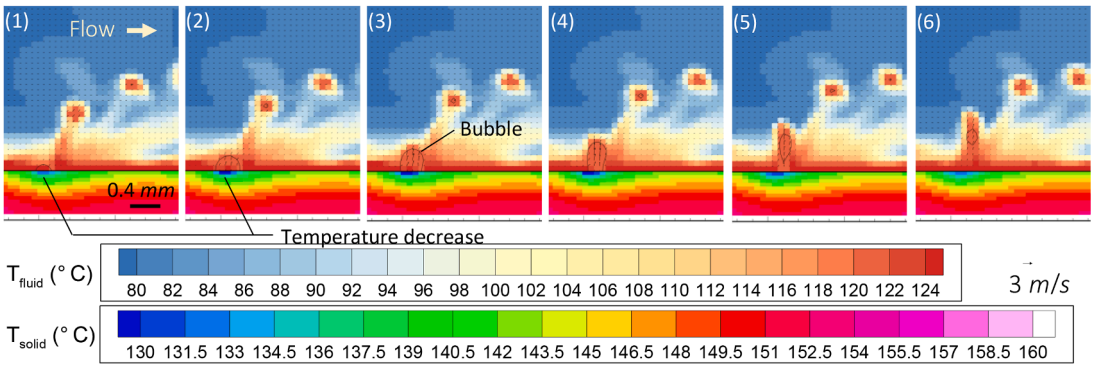

Fig. 28. Evolution of bubble and temperature distributions in a Y-constant plane, visualized at 6000 *fps*.

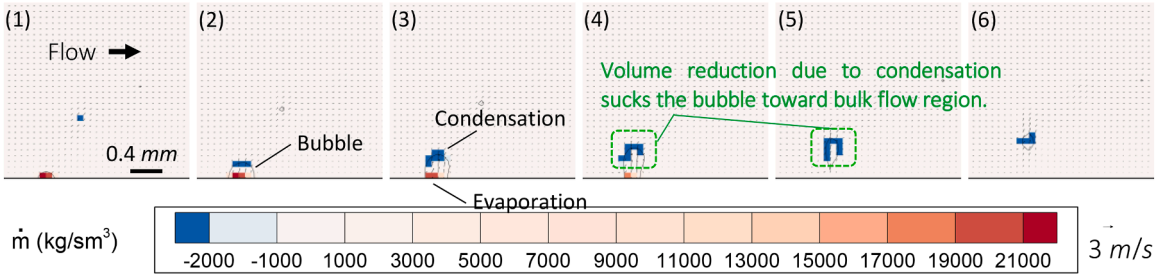

Fig. 29. Evolution of bubble (black line) and mass transfer distributions (color) in a Y-constant plane, visualized at 6000 *fps*.

et al. (2013), and sliding and lift off were well reproduced in the CFD simulations.

The feature of the bubble motion measured and simulated in the present study, i.e. lift off without any apparent sliding motion, has also been reported by Van Helden et al. (1995), though the degree of subcooling is not mentioned in the paper. The authors considered that the temperature difference in the liquid phase between the near-wall and bulk flow regions results in a change in the surface tension coefficient, which produces a Marangoni flow (Burdon, 2014), which was assumed to induce lift off. They named the force induced by the Marangoni flow *the temperature drop force*.

In contrast, the Marangoni force is not modelled in the present simulation, since the Continuum Surface Force, CSF, model is employed for the surface tension force, which cannot take into account this effect (Brackbill et al., 1992). However, the bubble dynamics, i.e. lift-off without sliding, shows good agreement with the measurement, which appears to imply that the Marangoni effect is not the main driving force in the lift-off phenomenon. What is considered important in the present work is the condensation that takes place at the top of the bubble, i.e. that close to the central, subcooled flow, as visualized in Fig. 29 (3)-(5). The condensation and associated shrinkage of volume at the "top" of the bubble, "sucks" the bubble into the bulk, triggering the lift-off event.

5. Conclusions

In this paper, we have investigated subcooled forced convection boiling flow around a heated rod at 2 *bar*, as measured in the COSMOS-L facility, and computed using a CFD simulation tool. The ultimate goal of the study is to increase understanding of the mechanism of DNB-type CHF, and the direct prediction of it via numerical simulation. As a first step, a flow with an applied heat flux of 50% CHF has been investigated, to evaluate the capabilities and limitations of CFD simulation tools currently being applied to the phenomenon. Since DNB is essentially a transient, local phenomenon, methods are needed that can resolve the boiling flow situation with sufficient space and time resolution; this is true both for the measurement techniques and for the simulation. In the COSMOS-L experiment, a high-speed camera was used to capture the bubble dynamics, LDA was employed to measure the bubble velocities, and shadowgraphy used to estimate the bubble-size distribution. The water quality, flowrate, inlet temperature and heater power were strictly controlled during the experiment, and the temperature distribution of the heater rod monitored using 12 thermocouples.

In the CFD simulation, an interface-tracking scheme was employed to capture the vapor/liquid boundaries, together with a sharp-interface phase-change model and a micro-layer model, as described in earlier works. As a boundary condition at the heat-transfer surface, an empirical correlation for nucleation site density, based on the Kocamustafaogullari and Ishii model, was employed, since the nucleation site density was not specifically measured in the experiment. This introduced uncertainties into the simulation. Ideally, the phase-change model requires at least 4~5 computational cells to capture the thermal boundary layer around the liquid-vapor interface. But we could not achieve this requirement, since the thermal boundary layer is too thin in this application, as a result of the subcooled boiling flow, even though we have used a supercomputer for the numerical simulation. Nonetheless, the CFD results have been compared with measurement, in order to clarify the limitations of the current CFD interface-tracking algorithm for applications of this type. Good agreement has been obtained for the wall temperatures at all the available measurement points, i.e. at six different elevations. This implies that the total heat transfer at the wall, which includes the heat transfer due to single-phase liquid, evaporation, sliding of bubbles along the wall and quenching, were all computed appropriately.

Consequently, we expect to learn the following from this paper:

- The kind of data that can be obtained using a state-of-the-art measurement system consists of a test section incorporating large optical windows, LDA, shadowgraphy, thermocouples, and a high-speed camera. This last produces highly resolved photos of subcooled convective nucleate boiling at the high frequency of 6000 fps, together with transient data concerning bubble velocities, bubble size distributions and temperature profiles.

- The CFD simulation, with interface tracking, can provide a three-dimensional distribution of the flow field, including velocity, pressure, temperature, void and mass transfer rate distributions.
- Based on the measurement and simulation data collected, the bubble dynamics at bubble nucleation and lift off can be uniquely clarified.
- Direct comparison between measurement and simulation reveals the limitations of the CFD simulation: i.e. overprediction of bubble merging and underprediction of the condensation process in the bulk flow, due to too coarse a computational grid being employed, this as a result of the complexity of the physics, and restricted computa-tional capability.

CRediT authorship contribution statement

Florian Kaiser: Investigation, Methodology, Validation, Writing – original draft. **Yohei Sato:** Methodology, Software, Validation, Writing – original draft, Writing – review & editing. **Stephan Gabriel:** Conceptualization, Funding acquisition, Methodology, Resources, Supervision, Writing – original draft, Writing – review & editing.

Declaration of competing interest

The authors declare the following financial interests/personal relationships which may be considered as potential competing interests:

Stephan Gabriel reports financial support was provided by the German Society for Plant and Reactor Safety (GRS) Projekt No. 1501473B. If there are other authors, they declare that they have no known competing financial interests or personal relationships that could have appeared to influence the work reported in this paper.

Data availability

Data will be made available on request.

Acknowledgements

The authors would like to thank the former colleague Dr B. Smith for many valuable discussions, English corrections and for his careful reading of the final manuscript. This work was partially supported by a
grant from the Swiss National Supercomputing Centre (CSCS) under project ID psi05. Furthermore, part of the experimental work was carried out as part of the NUBEKS BMWi 1501473B project. **References**

Badillo, A., 2012. Quantitative phase-field modeling for boiling phenomena. Phys. Rev. E
86, 041603.
Brackbill, J.U., Kothe, D.B., Zemach, C., 1992. A continuum method for modeling surface tension. J. Comput. Phys. 100, 335–354.
Bruder, M., Sembach, L., Lampl, D., Hirsch, C., Sattelmayer, T., 2019. Local measurements on vertical subcooled flow boiling of refrigerant Novec 649. Int. J. Multiphase Flow 119, 108–122.
Burdon, R.S., 2014. Surface Tension and the Spreading of Liquids, paperback ed. Cambridge University Press, Cambridge.
Büttner, F., Heiler, W., Gabriel, S., Kuhn, D., 2018. Experimental investigation of bubble entrainment by a vertical jet plunging into a liquid water pool, Flüssigbad eintauchenden Freistrahl. Vortrag gehalten auf 26. Fachtagung Experimentelle Strömungsmechanik (2018), Rostock, Germany.
Chorin, A.J., 1968. Numerical solution of the Navier-Stokes equations. Math. Comput. 22, 745–762.
Cifani, P., Kuerten, J.G.M., Geurts, B.J., 2018. Highly scalable DNS solver for turbulent bubble-laden channel flow. Comput. Fluids. 172, 67–83.
Courant, R., Friedrichs, K., Lewy, H., 1928. Über die partiellen Differenzengleichungen der mathematischen Physik. Math. Ann. 100, 32–74.
Coyajee, E., Boersma, B.J., 2009. Numerical simulation of drop impact on a liquid–liquid interface with a multiple marker front-capturing method. J. Comput. Phys. 228, 4444–4467.
Dhir, V.K., 1998. Boiling heat transfer. Annu Rev. Fluid. Mech. 30, 365–401. Esmaeeli, A., Tryggvason, G., 2004. Computations of film boiling. Part I: numerical method. Int. J. Heat. Mass Transf. 47, 5451–5461.
Ferziger, J.H., Perić, M., 2002. Methods for Unsteady Problems. In: Ferziger, J.H., Perić, M. (Eds.), Computational Methods for Fluid Dynamics. Springer Berlin Heidelberg, Berlin, Heidelberg, pp. 135–156.
Fischer, F., Hampel, U., 2010. Ultra fast electron beam X-ray computed tomography for two-phase flow measurement. Nucl. Eng. Des. 240, 2254–2259.
Fuchs, T., Kern, J., Stephan, P., 2006. A transient nucleate boiling model including microscale effects and wall heat transfer. J. Heat. Transfer. 128, 1257–1265. Gabriel, S., Schulenberg, T., Albrecht, G., Heiler, W., Miassoedov, A., Kaiser, F., Wetzel, T., 2018. Optical void measurement method for stratified wavy two phase flows. Exp. Therm. Fluid. Sci. 97, 341–350.
Gabriel, S.G., 2014. Experimental investigation of droplet separation in a horizontal countercurrentair/water stratified flow. KIT Scientific Publishing, Karlsruhe. Gaertner, R.F., 1965. Photographic study of nucleate pool boiling on a horizontal surface. J. Heat. Transfer. 87, 17–27.
Giustini, G., Walker, S.P., Sato, Y., Niceno, B., 2017. Computational fluid dynamics analysis of the transient cooling of the boiling surface at bubble departure. J. Heat. Transfer. 139, 091501.
Gong, S., Cheng, P., 2015. Lattice Boltzmann simulations for surface wettability effects in saturated pool boiling heat transfer. Int. J. Heat. Mass Transf. 85, 635–646.
Gong, S., Cheng, P., 2016. Two-dimensional mesoscale simulations of saturated pool boiling from rough surfaces. Part II: Bubble interactions above multi-cavities. Int. J. Heat. Mass Transf. 100, 938–948.
Gunther, F.C., 1950. Photographic study of surface-boiling heat transfer to water with forced convection.
Haas, C., 2012. Critical heat flux for flow boiling of water at low pressure on smooth and
micro-structured zircaloy tube surfaces. KIT.
Haas, C., Kaiser, F., Schulenberg, T., Wetzel, T., 2018. Critical heat flux for flow boiling of water on micro-structured Zircaloy tube surfaces. Int. J. Heat. Mass Transf. 120, 793–806.
Harlow, F.H., Welch, J.E., 1965. Numerical calculation of time-dependent viscous incompressible flow of fluid with free surface. Physics of Fluids 8, 2182–2189. Hibiki, T., Ishii, M., 2003. Active nucleation site density in boiling systems. Int. J. Heat. Mass Transf. 46, 2587–2601.
Huber, G., Tanguy, S., Sagan, M., Colin, C., 2017. Direct numerical simulation of nucleate pool boiling at large microscopic contact angle and moderate Jakob number. Int. J. Heat. Mass Transf. 113, 662–682.
Jamet, D., Lebaigue, O., Coutris, N., Delhaye, for the direct numerical simulation of liquid-vapor flows with phase change. J.M., 2001. The second gradient method J. Comput. Phys. 169, 624–651.
Kharangate, C.R., Mudawar, I., 2017. Review of computational studies on boiling and condensation. Int. J. Heat. Mass Transf. 108, 1164–1196.
Klausner, J.F., Mei, R., Bernhard, D.M., Zeng, L.Z., 1993. Vapor bubble departure in forced convection boiling. Int. J. Heat. Mass Transf. 36, 651–662.
Kocamustafaogullari, G., Ishii, M., 1983. Interfacial area and nucleation site density in boiling systems. Int. J. Heat. Mass Transf. 26, 1377–1387.
Kossolapov, A., 2021. Experimental investigation of subcooled flow boiling and CHF at prototypical pressures of light water reactors. Nuclear Science and Engineering. Massachusetts institute of technology.
Kunkelmann, C., Stephan, P., 2009. CFD simulation of boiling flows using the volume-of- fluid method within OpenFOAM. Numerical Heat Transfer, Part A: Applications 56, 631–646.
Kwakkel, M., Breugem, W.-P., Boersma, B.J., 2013. Extension of a CLSVOF method for droplet-laden flows with a coalescence/breakup model. J. Comput. Phys. 253, 166–188.
Lee, R.C., Nydahl, J.E., 1989. Numerical calculation of bubble growth in nucleate boiling from inception through departure. J. Heat. Transfer. 111, 474–479.
Lemmert, M., Chawla, J.M., 1977. Influence of flow velocity on surface boiling heat transfer coefficient. In: Hahne, E., Grigull, U. (Eds.), Heat transfer in boiling. Academic Press.
Levy, S., 1959. Generalized correlation of boiling heat transfer. J. Heat. Transfer. 81, 37–42.
Li, A., Ahmadi, G., Bayer, R.G., Gaynes, M.A., 1994. Aerosol particle deposition in an obstructed turbulent duct flow. J. Aerosol. Sci. 25, 91–112.
Li, D., Dhir, V.K., 2007. Numerical study of single bubble dynamics during flow boiling. J. Heat. Transfer. 129, 864–876.
Li, Q., of Kang, boiling Q.J., heat Francois, transfer: The M.M., He, boiling Y.L., curve Luo, and K.H., the 2015. effects of Lattice wettability. Boltzmann Int. J. modeling Heat. Mass Transf. 85, 787–796.
Lilly, D.K., 1967. The representation of small-scale turbulence in numerical simulation experiments. In: IBM sci. comp. symp. on environmental sciences. New York.
Lorensen, W., Cline, H., 1987. Marching cubes: A high resolution 3D surface construction algorithm. In: SIGGRAPH '87: Proceedings of the 14th Annual Conference on Computer Graphics and Interactive Techniques. ACM, pp. 163–169.
Maity, S., 2000. Effect of velocity and gravity on bubble dynamics. University of California, Los Angeles.
Mittal, R., Iaccarino, G., 2005. Immersed boundary methods. Annu Rev. Fluid. Mech. 37, 239–261.
Murallidharan, J., Giustini, G., Sato, Y., Ničeno, B., Badalassi, V., Walker, S.P., 2016. Computational fluid dynamic simulation of single bubble growth under high-pressure pool boiling conditions. Nucl. Eng. Technol. 48, 859–869.
Nakamura, T., Tanaka, R., Yabe, T., Takizawa, K., 2001. Exactly conservative semi-Lagrangian scheme for multi-dimensional hyperbolic equations with directional splitting technique. J. Comput. Phys. 174, 171–207.
Prasser, H.M., 1999. Wire-mesh sensors for two-phase flow investigations. Forschungszentrum Rossendorf, Germany, pp. 23–28.
Rohsenow, W.M., 1971. Boiling. Annu Rev. Fluid. Mech. 3, 211–236.

Sato, Y., Lal, S., Niceno, B., 2013. Computational fluid dynamics simulation of single bubble dynamics in convective boiling flows. Multiphase Sci. Technol. 25, 287–309.
Sato, Y., Niceno, B., 2012. A conservative local interface sharpening scheme for the constrained interpolation profile method. Int. J. Numer. Methods Fluids. 70, 441–467.
Sato, Y., Niceno, B., 2013. A sharp-interface phase change model for a mass-conservative interface tracking method. J. Comput. Phys. 249, 127–161.
Sato, Y., Niceno, B., 2015. A depletable micro-layer model for nucleate pool boiling. J. Comput. Phys. 300, 20–52.
Sato, Y., Niceno, B., 2017. Nucleate pool boiling simulations using the interface tracking method: Boiling regime from discrete bubble to vapor mushroom region. Int. J. Heat. Mass Transf. 105, 505–524.
Sato, Y., Niceno, B., 2018. Pool boiling simulation using an interface tracking method: From nucleate boiling to film boiling regime through critical heat flux. Int. J. Heat. Mass Transf. 125, 876–890.
Sato, Y., Smith, B.L., Niceno, B., 2018. Examples of Pool-Boiling Simulations Using an Interface Tracking Method Applied to Nucleate Boiling, Departure from Nucleate Boiling and Film Boiling, Encyclopedia of Two-Phase Heat Transfer and Flow III. WORLD SCIENTIFIC, pp. 225–263.
Smagorinsky, J., 1963. General circulation experiments with the primitive equations. Mon. Weather. Rev. 91, 99–164.
Son, G., Dhir, V.K., 2008. Numerical simulation of nucleate boiling on a horizontal surface at high heat fluxes. Int. J. Heat. Mass Transf. 51, 2566–2582.
Son, G., Dhir, V.K., Ramanujapu, N., 1999. Dynamics and heat transfer associated with a single bubble during nucleate boiling on a horizontal surface. J. Heat. Transfer. 121, 623–631.
Stäbler, T., 2007. Experimentelle Untersuchung und physikalische Beschreibung der Schichtenströmung in horizontalen Kanälen. Karlsruhe Institute of Technology. Takada, N., Tomiyama, A., 2007. Numerical simulation of isothermal and thermal two-phase flows using phase-field modeling. Int. J. Mod. Phys. C 18, 536–545. Tompkins, C., Prasser, H.-M., Corradini, M., 2018. Wire-mesh sensors: a review of methods and uncertainty in multiphase flows relative to other measurement techniques. Nucl. Eng. Des. 337, 205–220.
Tritton, D.J., 1977. Thermal Flows: Basic Equations and Concepts. In: Tritton, D.J. (Ed.), Physical Fluid Dynamics. Springer, Netherlands, Dordrecht, pp. 127–134.
Utaka, Y., Kashiwabara, Y., Ozaki, M., 2013. Microlayer structure in nucleate boiling of water and ethanol at atmospheric pressure. Int. J. Heat. Mass Transf. 57, 222–230.
Van Helden, W.G.J., Van Der Geld, C.W.M., Boot, P.G.M., 1995. Forces on bubbles growing and detaching in flow along a vertical wall. Int. J. Heat. Mass Transf. 38, 2075–2088.
Wang, J., Wang, H., Xiong, J., 2023. Experimental investigation on microlayer behavior and bubble growth based on laser interferometric method. Front. Energy Res. 11.
Welch, S.W.J., 1998. Direct simulation of vapor bubble growth. Int. J. Heat. Mass Transf. 41, 1655–1666.
Welch, S.W.J., Wilson, J., 2000. A volume of fluid based method for fluid flows with phase change. J. Comput. Phys. 160, 662–682.
Xiao, F., Yabe, T., Ito, T., 1996. Constructing oscillation preventing scheme for advection equation by rational function. Comput. Phys. Commun. 93, 1–12.
Yadigaroglu, G., 2005. Computational Fluid Dynamics for nuclear applications: from CFD to multi-scale CMFD. Nucl. Eng. Des. 235, 153–164.